The formation of CO2 through consumption of gas-phase CO on vacuum-UV irradiated water ice

Terwisscha van Scheltinga, J.; Ligterink, N.F.W.; Bosman, A.D.; Hogerheijde, M.R.; Linnartz, H.

Document Version
Final published version

Link to publication

Astronomy & Astrophysics

The formation of CO_2 through consumption of gas-phase CO on vacuum-UV irradiated water ice

J. Terwisscha van Scheltinga[1,2,★] , N. F. W. Ligterink[3] , A. D. Bosman[4] , M. R. Hogerheijde[2,5] , and H. Linnartz[1]

[1] Laboratory for Astrophysics, Leiden Observatory, Leiden University, PO Box 9513, 2300 RA Leiden, The Netherlands
e-mail: `jeroentvs@virginia.edu`
[2] Leiden Observatory, Leiden University, PO Box 9513, 2300 RA Leiden, The Netherlands
[3] Physics Institute, University of Bern, Sidlerstrasse 5, 3012 Bern, Switzerland
[4] Department of Astronomy, University of Michigan, 323 West Hall, 1085 S. University Avenue, Ann Arbor, MI 48109, USA
[5] Anton Pannekoek Institute for Astronomy, University of Amsterdam, Science Park 904, 1098 XH Amsterdam, The Netherlands

ABSTRACT

Context. Recent observations of protoplanetary disks suggest that they are depleted in gas-phase CO up to a factor of 100 with respect to predictions from physical–chemical (or thermo-chemical) models. It has been posed that gas-phase CO is chemically consumed and converted into less volatile species through gas-grain processes. Observations of interstellar ices reveal a CO_2 component in a polar (H_2O) ice matrix, suggesting potential co-formation or co-evolution.
Aims. The aim of this work is to experimentally verify the interaction of gas-phase CO with solid-state OH radicals on the surface of water ice above the sublimation temperature of CO.
Methods. Amorphous solid water (ASW) is deposited in an ultra-high vacuum (UHV) setup at 15 K and irradiated with vacuum-UV (VUV) photons (140–170 nm, produced with a microwave-discharge hydrogen-flow lamp) to dissociate H_2O and create OH radicals. Gas-phase CO is simultaneously admitted and only adsorbs with a short residence time on the ASW. Formed products in the solid state are studied in the infrared through Fourier transform infrared spectroscopy and once released into the gas phase with quadrupole mass spectrometry.
Results. Our experiments show that gas-phase CO is converted into CO_2 when interacting with ASW that is VUV irradiated with a conversion efficiency of 7–27%. Between 40 and 90 K, CO_2 production is constant, above 90 K, CO_2 production is reduced in favor of O_2 production. In the temperature range of 40–60 K, the CO_2 remains in the solid state, while at temperatures ≥70 K the majority of the formed CO_2 is immediately released into the gas phase.
Conclusions. We conclude that gas-phase CO reacts with OH radicals, created on the surface of ASW with VUV irradiation, above its canonical sublimation temperature. The diffusion during the short, but nonzero, residence times of CO on the surface of ASW suggests that a Langmuir-Hinshelwood type reaction is involved. This gas-phase CO and solid-state OH radical interaction could explain (part of) the observed presence of CO_2 embedded in water-rich ices when it occurs during the build up of the H_2O ice mantle. It may also contribute to the observed lack of gas-phase CO in planet-forming disks, as previously suggested. It should be noted though that our experiments indicate a lower water ice dissociation efficiency than originally adopted in model descriptions of planet-forming disks and molecular clouds. Incorporation of the reduced water ice dissociation and increased binding energy of CO on a water ice surfaces in physical–chemical models would allow investigation of this gas-grain interaction to its full extend.

Key words. astrochemistry – molecular processes – protoplanetary disks – ISM: clouds – methods: laboratory: molecular – methods: laboratory: solid state

1. Introduction

In typical laboratory astrochemistry experiments, the processes that occur in the solid state and gas phase are investigated independently. However, there are conditions in the interstellar medium where these are intimately intertwined and could affect each other. In this work, we explore experimentally the interaction between gas-phase carbon monoxide (CO) and UV irradiated water (H_2O) ice and place the results in astrophysical context.

In the study of planet forming disks, CO and its isotopologues are common tracers of the total gas mass, but are often found to be depleted by factors up to 10–100, even after taking into account freeze-out of CO in the coldest disk regions (Ansdell et al. 2016; Miotello et al. 2017; Trapman et al. 2021). Recent physical–chemical models suggest that gas-phase CO could be converted into CO_2 after interaction with a UV-irradiated H_2O ice surface, at temperatures just above the CO sublimation temperature (Drozdovskaya et al. 2016; Eistrup et al. 2016; Bosman et al. 2018). Under realistic disk conditions, this pathway was found by Bosman et al. (2018) to convert significant amounts of gas-phase CO into CO_2. However, little experimental work exists to confirm this process. If efficient, the UV-irradiated edges of molecular clouds could be another environment where this gas-grain reaction can occur. This possibly explains (part of) the observed presence of CO_2 in polar ices (see e.g., Gerakines et al. 1999; Pontoppidan et al. 2008), if gas-phase CO conversion happens on the grain surface during the build up of the H_2O ice mantle, adding to contributions from other CO_2 formation pathways already studied.

★ Current address: Department of Astronomy, University of Virginia, PO Box 400325, Charlottesville, VA 22904, USA

The solid-state formation of CO_2 has been investigated both theoretically (see e.g., Goumans et al. 2008; Goumans & Andersson 2010; Arasa et al. 2013) and experimentally. Several energetic and non-energetic pathways have been experimentally confirmed to form CO_2 under astrophysical conditions, such as, ground-state CO reacting with an electronically excited CO* to form CO_2 and atomic carbon (Gerakines et al. 1996; Palumbo et al. 1998; Loeffler et al. 2005; Jamieson et al. 2006; Bennett et al. 2009; Ioppolo et al. 2009), CO reacting with atomic oxygen to form CO_2 (Roser et al. 2001; Madzunkov et al. 2006; Raut & Baragiola 2011; Ioppolo et al. 2013; Minissale et al. 2013), CO reacting with a hydroxyl (OH) radical to form CO_2 and atomic hydrogen (Watanabe & Kouchi 2002b; Watanabe et al. 2007; Ioppolo et al. 2009, 2011; Oba et al. 2010, 2011; Noble et al. 2011; Zins et al. 2011; Yuan et al. 2014), formaldehyde (H_2CO) reacting with atomic oxygen and to form CO_2 and molecular hydrogen (Minissale et al. 2015), or oxidation of carbonaceous surfaces (Mennella et al. 2006; Fulvio et al. 2012; Raut et al. 2012; Sabri et al. 2015; Shi et al. 2015).

The above pathways were found to significantly produce CO_2 in the solid state and only the last two pathways do not include CO. The majority of these solid-state experiments are performed at temperatures below 20 K, representative of dark cloud or disk midplane (>20 AU) conditions. This is well below the CO sublimation temperature, which is approximately 20 and 30 K for interstellar and laboratory timescales, respectively (see e.g., Fayolle et al. 2011; Schwarz et al. 2016). The low temperatures in these experiments ensure that CO stays adsorbed on the surface and is able to react with the other ice constituents. The experimental studies by Oba et al. (2011) and Yuan et al. (2014) have investigated the formation of CO_2 from CO at substrate temperatures above the sublimation temperature of CO. In the former, CO_2 was formed when CO and OH radicals were co-deposited on a substrate in the temperature range from 40 to 60 K. The latter observed formation of CO_2 when gas-phase CO interacted with OH radicals produced by UV photons on the surface of water ice at 76 K. Both works show that CO can interact with OH radicals in the solid state above its canonical desorption temperature.

In this work, we set out to experimentally investigate the conversion of gas-phase CO into CO_2 on the surface of vacuum-UV (VUV) irradiated water ice (40–120 K), and assess the efficiency in astrophysical settings. Specifically, amorphous solid water (ASW) is irradiated at a temperature of ≥40 K, which ensures that the majority of the gas-phase CO in our experimental chamber does not freeze out onto our ASW sample. Section 2 describes the methods used to investigate this process, and analyze the data. Results are presented in Sect. 3 and are discussed in Sect. 4. The astrophysical implications are given in Sect. 5, and concluding remarks are summarized in Sect. 6.

2. Methods

2.1. CryoPAD2

All reported laboratory measurements are performed in the Leiden Laboratory for Astrophysics using the Cryogenic Photoproduct Analysis Device 2 (CryoPAD2; Ligterink et al. 2017, 2018b). This setup operates under ultra-high vacuum conditions ($P_{mc} \sim 5 \times 10^{-11}$ mbar at 15 K). It accommodates a gold-coated substrate which is positioned in the center of a stainless steel chamber and acts as an analogue for an interstellar dust-grain surface. On top of the chamber a closed-cycle helium cryostat is positioned which cools the gold-coated surface down to

temperatures of 15 K. A Lakeshore 350 temperature controller sets the temperature of the substrate through PID-controlled Joule heating in the range of 15–300 K with an absolute and relative accuracy of ±2 and ±1 K, respectively. In order to further simulate the interstellar environments in which these dust grains reside, a microwave-discharge hydrogen-flow lamp (MDHL) is connected to the chamber. These type of sources generally produce VUV photons at 121.6 nm, Lyman-α, and between 140 and 170 nm, which corresponds to photon energies of 7.5–10.2 eV. However, in the present experiments a MgF_2 window is used which absorbs Lyman-α photons, see Appendix A for the VUV spectrum. The flux of the MDHL at the location of the substrate is determined with a NIST-calibrated photodiode (SXUV-100) as $(2.5 \pm 0.3) \times 10^{14}$ photons s^{-1} cm^{-2}.

The reactions induced by VUV irradiation under these conditions are diagnosed using infrared spectroscopy and mass spectrometry. The collimated beam of a Fourier-Transform InfraRed Spectrometer (Agilent 660 FTIRS) is used for Reflection Absorption InfraRed Spectroscopy (RAIRS). In this method the incoming FTIR beam is reflected from the substrate under a grazing incidence angle, improving the sensitivity. This in situ diagnostic allows us to probe, qualitatively and quantitatively, the molecular content in the ice adsorbed on the substrate. The infrared spectra are acquired continuously during the experiments to investigate and track the chemical evolution in the solid state under the influence of VUV irradiation.

The second diagnostic tool is a Hiden HAL/3F PIC 1000 series quadrupole mass spectrometer (QMS). During VUV irradiation some molecular species desorb from the substrate into the gas phase. The QMS probes the molecular content of the atmosphere in the chamber. This allows for qualitative assignment of species released or produced during the experiments through their characteristic mass-fragmentation patterns. Furthermore, after calibration of the QMS through the procedure described in Sect. 2.3.2, it is possible to derive the quantitative amount of a species released into the gas phase. After VUV irradiation, the substrate temperature is linearly increased with time in a temperature programmed desorption (TPD) experiment until all adsorbed species have thermally desorbed. During TPD, species are released into the gas phase at their canonical desorption temperature, and are subsequently measured by the QMS. Upon ionization, in our case with 70 eV electrons, molecules fragment into a characteristic fragmentation pattern, which allows for assignment of newly formed species, complementary to the infrared. Rare isotopologue precursors are used to discriminate from background gas contaminations, and to add diagnostic information to the RAIRS and TPD experiments.

2.2. Experimental protocol

The following molecules are used in the experiments: Milli-Q H_2O (Type I), $H_2^{18}O$ (Sigma-Aldrich, 97%), regular CO (Linde gas, 99.997%), and $^{13}C^{18}O$ (Sigma-Aldrich, 99% ^{13}C and 95% ^{18}O). The experiment is started by depositing a layer of ASW onto the substrate. The gas-phase H_2O enters the chamber roughly 1 cm away from the substrate, and is deposited under normal incidence to the substrate through a capillary array. The temperature of the substrate during H_2O deposition is set at 15 K and the water ice is deposited for 10 minutes. This ensures that the deposited H_2O is porous-ASW. A precision leak valve is used to guarantee consistent column densities of H_2O throughout the experiments. Before the experiments continue, the chamber is left to settle for at least 30 minutes. This ensures that the pressure

J. Terwisscha van Scheltinga et al.: CO_2 production through gas-phase CO consumption on VUV irradiated water ice

Table 1. Overview of performed experiments.

Series	Molecules	Temperature [a] (K)	H_2O column density [b,c] (ML)	Notes
Main experiments	$H_2^{18}O$ (s) + $^{13}C^{18}O$ (g)	40	57.8	–
	$H_2^{18}O$ (s) + $^{13}C^{18}O$ (g)	50	56.7	–
	$H_2^{18}O$ (s) + $^{13}C^{18}O$ (g)	60	57.6	–
	$H_2^{18}O$ (s) + $^{13}C^{18}O$ (g)	70	61.8	–
	$H_2^{18}O$ (s) + $^{13}C^{18}O$ (g)	80	62.9	–
	$H_2^{18}O$ (s) + $^{13}C^{18}O$ (g)	90	57.8	–
	$H_2^{18}O$ (s) + $^{13}C^{18}O$ (g)	100	56.8	–
	$H_2^{18}O$ (s) + $^{13}C^{18}O$ (g)	120	58.3	–
Control	$H_2^{18}O$ (s)	40	70.2	Water only
	$H_2^{18}O$ (s) + ^{13}CO (g)	60	63.2	$^{13}C^{16}O$
	$H_2^{18}O$ (s) + $^{13}C^{18}O$ (g)	40	66.4	No VUV irradiation

Notes. [a]All ices have been deposited at 15 K. The temperature refers to the value at which the ASW is VUV irradiated. [b]The H_2O column density is derived through the integrated area of the OH-stretching mode (boundaries, 3800–2950 cm^{-1}) through Eq. (1), where A' is taken to be 1.5×10^{-16} cm molecule^{-1} ($H_2^{16}O$, Bouilloud et al. 2015). [c]It is likely that this value represents a lower limit due to the nonlinearity of RAIRS at column densities above 10 ML.

in the main chamber (P_{mc}) is below 2.0×10^{-10} mbar and that the amount of residual gas-phase H_2O can be neglected. After this, the substrate temperature is slowly increased, with a rate of 2 K min^{-1}, to the temperature at which the experiments are performed. Once the desired sample temperature is reached, the MDHL is started and gas-phase CO is admitted into the chamber. The gas-phase CO enters the chamber at roughly 5 cm distance from the substrate, and under 45 degrees with respect to the substrate normal. The precision leak valve is set to have a constant P_{mc} of 5.0×10^{-8} mbar. This translates into the ASW surface being exposed to approximately 5×10^{13} CO molecules cm^{-2} s^{-1}. The ASW is exposed in total 300 minutes to VUV irradiation (with a total incident fluence of 4.5×10^{18} photons) and CO molecules, after which TPD is performed to sublimate parent and newly-formed species. During VUV irradiation, the shutter between the MDHL and vacuum chamber is closed periodically to measure the baseline signals of the chamber without VUV irradiation. The experiments performed in this study are listed in Table 1.

2.3. Data analysis

2.3.1. RAIRS vibrational spectroscopy

The infrared spectra are acquired in RAIRS mode with the FTIR and are subsequently analysed. The column density, $N_{species}$, of the probed molecules on the substrate is derived through the following relationship with the measured absorbance

$$N_{species} = \ln(10) \cdot \frac{\int_{band} \log_{10}\left(\frac{I_0(\tilde{\nu})}{I(\tilde{\nu})}\right) d\tilde{\nu}}{R \cdot A'}, \quad (1)$$

where the absorbance, the ratio of the incoming flux, $I_0(\tilde{\nu})$, and reflected flux, $I(\tilde{\nu})$, is integrated over a range that encompasses the full absorption feature, and A' is the apparent band strength. The apparent band strengths are taken from literature from transmission experiments; for RAIRS these values need to be corrected with a value R in order to retrieve accurate column densities. The RAIRS correction factor (R) is empirically determined on CryoPAD2 through isothermal desorption of CO and is found to be 4.5 (see e.g., Öberg et al. 2009;

Ligterink et al. 2018a, for a description of the used approach). We assume that the area probed by the infrared beam on our substrate amounts to 1.0 cm^2 and thus the amount of molecules, $N_{species}$, is also the column density, given in molecules cm^{-2}. As stated before and shown in Table 1, all main experiments are performed with $^{13}C^{18}O$ and $H_2^{18}O$ resulting in the formation of $^{13}C^{18}O_2$. To our knowledge the apparent band strength of this specific isotope of CO_2 is unknown and thus the apparent band strength of $^{13}CO_2$, 6.8×10^{-17} cm molecule^{-1} (Bouilloud et al. 2015), is used to approximate the column density of $^{13}C^{18}O_2$.

As is shown in Sect. 3, multiple CO_2 features are observed in the infrared. In order to follow the growth of these different CO_2 features, the three prominent ones are approximated by fitting a Gaussian profile to each of them in order to deconvolve the spectra. The CURVE_FIT function from SCIPY is used to fit a Gaussian profile to each absorption component through least squares regression (Virtanen et al. 2020). A 3-Gaussian fit reproduces the integrated absorbance to ≤10%, and suffices as a fit, given the variation in observed profile shapes due to (small) changes in physical or chemical environment and spectroscopic artifacts in the spectra.

2.3.2. QMS calibration

RAIRS allows determination of the column density in the solid state, while the QMS allows for quantification of molecules released from the solid state into the gas phase. In order to use the QMS for quantitative purposes, mass signals need to be calibrated and this is realized, through the photodesorption of CO (see e.g., Fayolle et al. 2013; Martín-Doménech et al. 2015). The loss of solid-state CO is traced with RAIRS and is correlated to the gas-phase CO signal measured simultaneous by the QMS. This calibration allows for the conversion of any measured gas-phase QMS signal, released under VUV irradiation, to a column density from the solid state. However, one needs to correct for the difference in the electron-impact ionization cross section, the fractional fragmentation, and the mass sensitivity of the QMS of the investigated molecule with respect to CO. The following equation is used to quantify the amount of

CO_2 formed in the solid state and subsequently released into the gas phase

$$\frac{N_{CO_2(ice)}}{\int S_{CO_2(gas)}} = \frac{\sigma_{CO}}{\sigma_{CO_2}} \cdot \frac{F(CO^+/CO)}{F(CO_2^+/CO_2)} \cdot \frac{M(CO)}{M(CO_2)} \cdot \frac{N_{CO(ice)}}{\int S_{CO(gas)}}, \quad (2)$$

where N_{CO_2} is the column density of CO_2 released from the solid state, $\int S_{CO_2}$ the integrated CO_2 QMS signal, σ the total electron-impact ionization cross section, F the fragmentation fraction of the ionized species, and M the mass sensitivity function of the Hiden QMS on CryoPAD2. The last term of Eq. (2) is the CO calibration experiment, where N_{CO} is the amount of CO that photodesorbed from the solid state and $\int S_{CO}$ the integrated CO signal measured by the QMS during photodesorption. In a similar fashion the column density of O_2 is determined, but with its respective parameters. The electron-impact ionization cross sections (σ) used in this work for CO, CO_2, and O_2 are 2.516, 3.521, and 2.441 Å^2 at 70 eV, respectively (Kim et al. 2004). The fragmentation fractions (F) for CO^+, CO_2^+, and O_2^+ are 0.940, 0.942, and 0.821, respectively, where unity is the normalized summation of all fragmentation fragments.

3. Results

In this section, we present the results of the experiments mentioned in Table 1. In general, irradiation of ASW with VUV photons in the presence of gas-phase CO produces CO_2. Additionally, in the experiments at the higher end of the temperature range, (>90 K), formation of molecular oxygen (O_2) is observed. To understand the processes that occur on or in the solid state we consider the infrared and QMS results, and how these change with temperature.

3.1. Infrared spectroscopy results

We observe the formation of CO_2 in the solid state through RAIRS. In Fig. 1, we present five difference RAIRS spectra at experimental temperatures of 40 and 60 K, in the top and bottom panel, respectively. Such spectra are obtained by subtracting the initial ASW spectrum, before VUV irradiation, from the subsequently acquired spectra during irradiation. The spectra shown here are obtained at five different VUV fluence intervals where ASW was simultaneously exposed to gas-phase CO. Although the main isotopes used are ^{13}C and ^{18}O, small amounts of ^{12}C and ^{16}O are present in our samples. It is apparent that in the wavenumber range 2350–2225 cm^{-1} absorption features grow with increasing fluence. All of the features in this range are attributed to isotopologues of CO_2. The three most distinct features are positioned at 2279, 2260, and 2243 cm^{-1} and are attributed to $^{13}C^{18}O_2$ aggregates on top of the water ice, $^{13}C^{16}O^{18}O$ bound to water, and $^{13}C^{18}O_2$ bound to water, respectively (Lehmann et al. 1977; He et al. 2017).

The lowest ASW temperature at which the experiments are performed is 40 K. This ensures that the majority of the gas-phase CO molecules that enter the vacuum chamber cannot adsorb onto our sample, as it is above the canonical desorption temperature of CO. However, as shown by He et al. (2016b), the sticking coefficient of CO on nonporous-ASW (np-ASW) is close to unity at 40 K. Once the ASW is covered with CO, no additional CO freeze-out occurs. This is also seen in our experiment at 40 K through the infrared signal around 2040 cm^{-1} where, preceding VUV-irradiation, the ASW is briefly exposed to gas-phase CO only (Fig. 1a). In this short 5 minute window, CO adsorbs on top of the ASW with a column density of
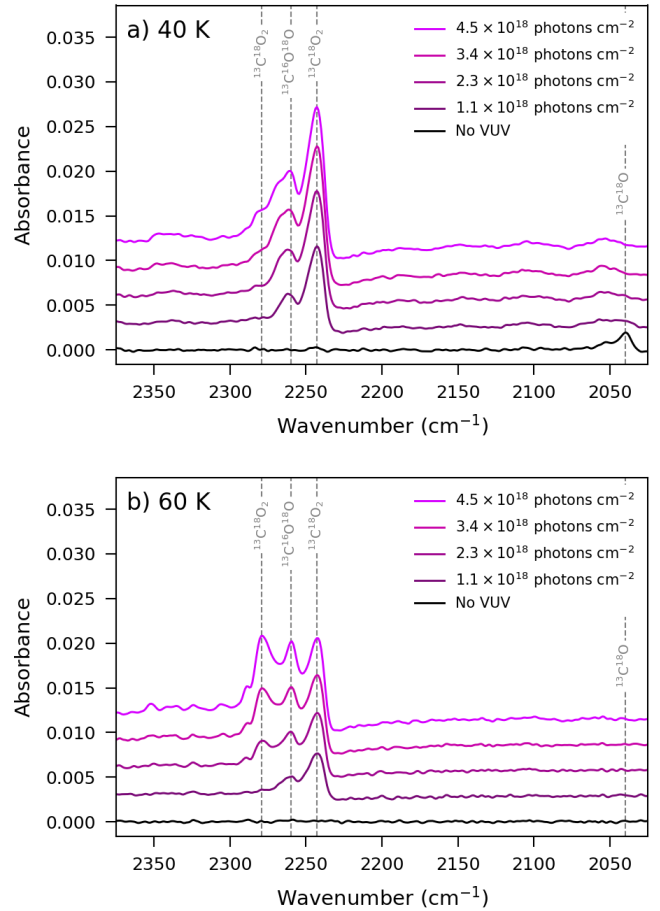

Fig. 1. Five difference RAIRS spectra following VUV irradiation of ASW ($H_2^{18}O$) at 40 K (*top*) and 60 K (*bottom*) with gas-phase $^{13}C^{18}O$ at different VUV fluences, increasing from low to high. The vertically dashed lines indicate the assignment of the main absorption features.

~1.1 ML, where 1 ML equals 10^{15} molecules cm^{-2}. This CO ice grows within 60 s and does not further increase. As soon as VUV irradiation starts, this solid-state CO on the surface of the ASW is converted into CO_2. At ASW temperatures ≥50 K no adsorption of CO is seen, illustrated here for a temperature of 60 K (Fig. 1b). This is expected as the sticking coefficient of CO on ASW significantly drops at temperatures ≥50 K. An upper limit of ≤0.1 ML is derived for CO adsorbed on top of ASW at temperatures ≥50 K.

Figure 2 shows the combined results of the experiment with ASW at 40 K. The upper panels show infrared data during irradiation (a) and after irradiation upon TPD (b). The lower panels (c and d) show the corresponding gas-phase data recorded with the QMS. Figure 2a shows the growth of each individual solid-state CO_2 component during VUV irradiation (shaded areas) as well as the combined results (red curve), while Fig. 2b shows the subsequent decrease during TPD after irradiation. It is evident that the deconvolved components evolve differently from each other. The CO_2 component at 2243 cm^{-1} is the first to grow and levels off as the VUV fluence increases. This component is attributed to $^{13}C^{18}O_2$ that initially forms and is bound to the ASW surface. Sequentially, aggregates start to form on top of the water ice as the column density of CO_2 increases, because CO_2 does not wet the ASW surface, that is, the binding energy between CO_2–CO_2 is higher than CO_2–H_2O (He et al. 2017). These CO_2 aggregates absorb infrared light at a different wavenumber, namely 2279 cm^{-1} (cf. He et al. 2017, who observed the same features,
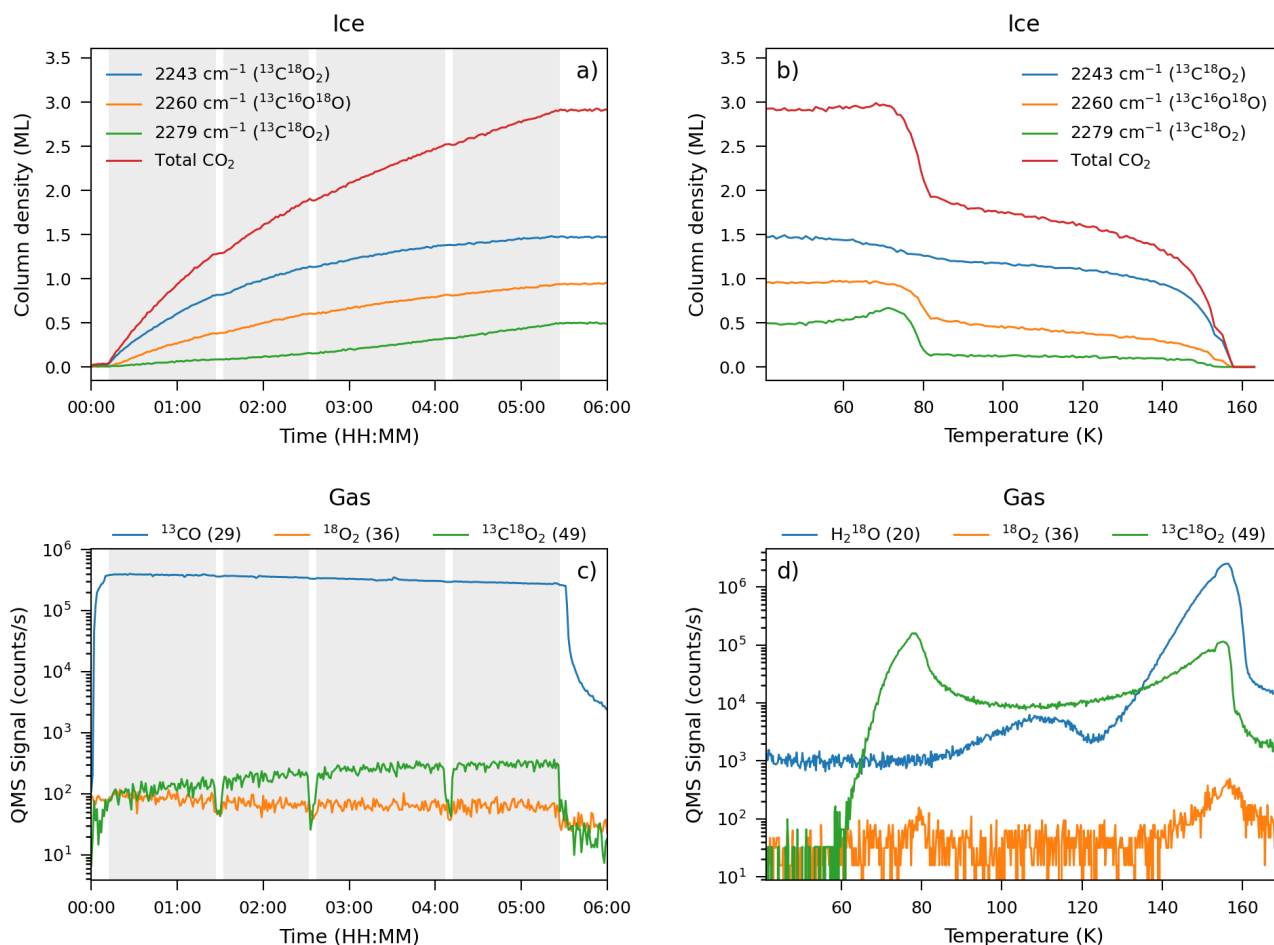
Fig. 2. Results of the experiment of ASW at a temperature of 40 K. In the *top row* the deconvolved infrared components, which trace the solid state, are given, based on RAIRS during VUV irradiation (*panel a*) and temperature programmed desorption (TPD) in *panel b*. In the *bottom row* the data from the quadrupole mass spectrometer (QMS) is presented, which trace the gas phase. The *left column* shows data acquired during VUV irradiation (shaded areas indicate when the VUV shutter is open) and on the right during TPD. In *panel c*, ^{13}CO is shown, as measuring the main isotopologue ($^{13}C^{18}O$) would saturate the QMS. The ^{16}O isotope is present in the CO sample at a level of 5%.

but shifted by $\sim$100 cm^{-1} due to the different isotopologue used). With increasing temperature of the ASW, the diffusion of CO_2 across the ASW increases. This increased diffusion results in earlier formation of CO_2 aggregates and the amount of molecules in these aggregates increases. This is confirmed by less CO_2 molecules bound to ASW in the 2243 cm^{-1} component with increasing temperature, see Figs. 2a (40 K), B.1a (50 K), and B.2a (60 K). The absorption feature at 2260 cm^{-1} is due to $^{13}C^{16}O^{18}O$, formed from isotope impurities, bound to the ASW surface and is super imposed on top of the two absorption features of $^{13}C^{18}O_2$. There is a nonzero baseline between the 2243 and 2279 cm^{-1} features due to the range of binding energies on the surface of H_2O with CO_2. As a result, the fitting of the 2260 cm^{-1} component comprises contributions from both the 2243 and 2279 cm^{-1} features. This makes an unique assignment and quantification of the 2260 cm^{-1} component difficult.

A decrease in the CO_2 column density is shown in Fig. 2b, following sublimation into the gas phase during TPD. The overall decrease as well as the decrease of the individual components are shown. The CO_2 sublimates in two steps, the first desorption event occurs at $\sim$80 K and the second at $\sim$155 K. The former is in line with the canonical desorption temperature of CO_2, and the latter with the canonical desorption temperature of H_2O. The component at 2279 cm^{-1} drops around $\sim$80 K, which is in line with aggregates of CO_2 on top of the water ice.

The component at 2243 cm^{-1} gradually drops as the temperature of the ASW increases and disappears with the desorption of H_2O at 156 K, which is in agreement with CO_2 bound to ASW surface.

At ASW temperatures $\geq$70 K, the majority of the formed CO_2 is immediately released back into the gas phase (see e.g., Fig. 3). At 70 and 80 K, however, some of the initially formed CO_2 remains in the solid state, see Fig. 3a and Appendix B.3a, respectively. This CO_2 is formed during the initial moments of VUV irradiation and is bound to the deep binding sites on the ASW surface that are able to "trap" CO_2. The column densities of this CO_2 at 70 and 80 K are 0.6 and 0.12 ML, respectively, compared to the $\sim$3 ML formed at temperatures below 70 K. No solid-state CO_2 is detected in the experiments with ASW temperatures $\geq$90 K, and the upper limit of solid-state CO_2 is derived to be $\leq$0.02 ML.

3.2. QMS results

The QMS allows for gas-phase species to be traced in the chamber during VUV irradiation and afterwards during TPD. The signals measured during TPD are only used for identification. In the following two sections we focus first on the QMS analysis of CO_2 that remained in the solid state (40–60 K) and then on CO_2 released into the gas phase ($\geq$70 K) after formation.
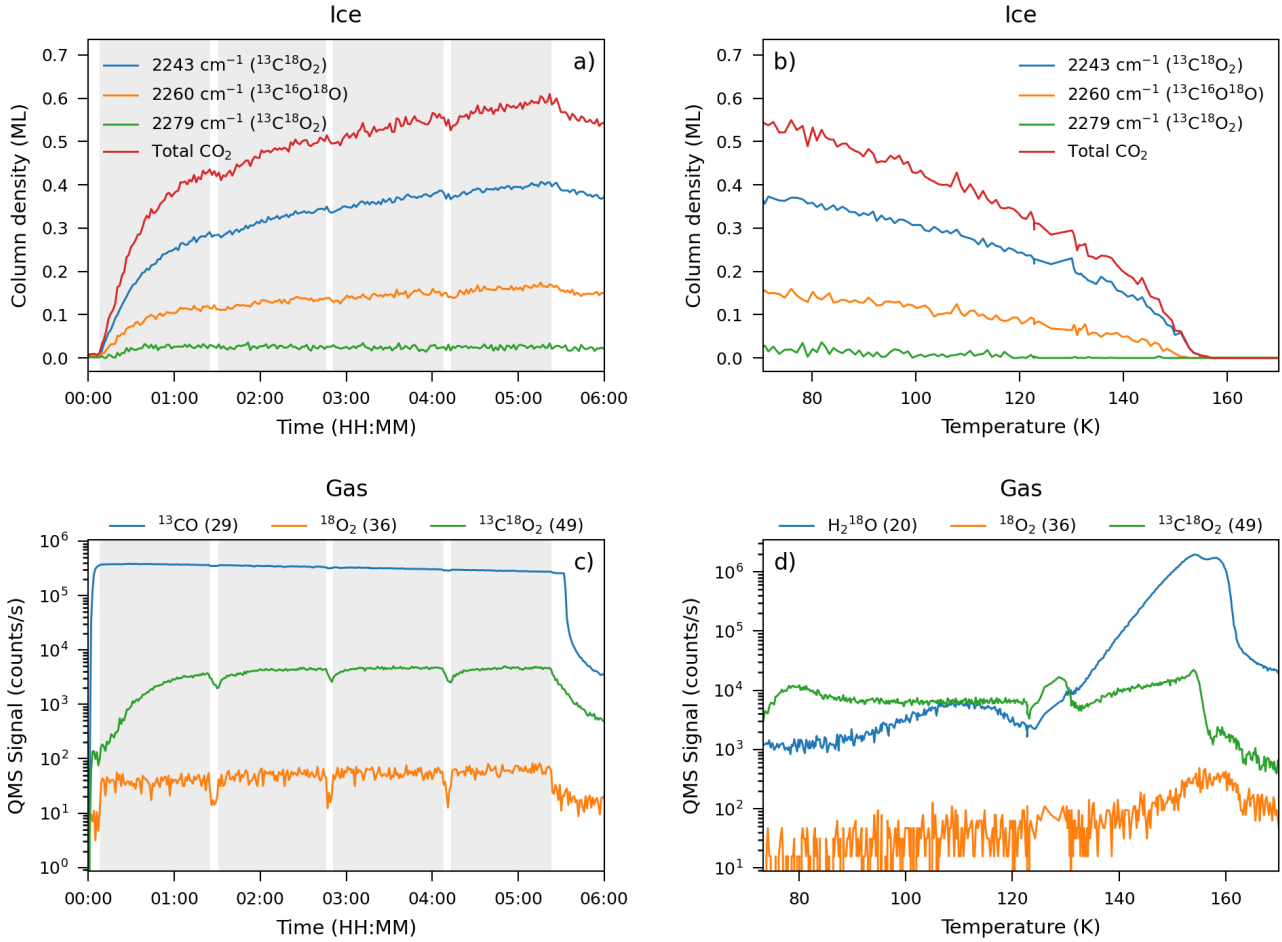
Fig. 3. Results of the experiment of ASW at a temperature of 70 K. In the top row, the deconvolved infrared components, which trace the solid state, are given, based on RAIRS during VUV irradiation (*panel a*) and temperature programmed desorption (TPD) in *panel b*. In the bottom row, the data from the quadrupole mass spectrometer (QMS) is presented, which trace the gas phase. The left column shows data acquired during VUV irradiation (shaded areas indicate when the VUV shutter is open) and on the right during TPD. In *panel c*, ^{13}CO is shown, as measuring the main isotopologue ($^{13}C^{18}O$) would saturate the QMS. The ^{16}O isotope is present in the CO sample at a level of 5%. The TPD QMS data in *panel d* between 120 and 130 K is unreliable due to a nonlinear temperature artifact during heating of the sample.

3.2.1. Solid-state CO_2 (40–60 K)

The majority of the CO_2 formed at ASW temperatures of 40–60 K remains in the solid state, as is found in the infrared experiments. This solid-state CO_2 is released into the gas phase during TPD due to thermal desorption, and subsequently measured with the QMS. However, during VUV irradiation there is some gas-phase CO_2 signal measured by the QMS. This is illustrated in Fig. 2c (shaded areas) by the signal at mass-to-charge ratio (m/z) = 49, which is associated with the main peak of the $^{13}C^{18}O_2$ mass spectrum. The increase in this CO_2 QMS signal follows approximately the same trend as the growth of the CO_2 column density measured in the infrared (Fig. 2a). When the VUV shutter is closed, non-shaded areas, the signal at m/z = 49 drops. We attribute this gas-phase CO_2 QMS signal to photodesorbed CO_2 from the solid state (Fillion et al. 2014).

During TPD, there are two distinct desorption peaks of CO_2 with an elevated plateau between them (see e.g., Fig. 2d). The first desorption peak occurs at 78 K, the canonical desorption temperature of CO_2. The CO_2 molecules that desorb at this temperature, are those in CO_2 aggregates. The second desorption peak coincides with the water desorption peak observed at 156 K. Both behave fully in agreement with the deconvolved infrared components at 2279 and 2243 cm^{-1} (see e.g., Fig. 2b).

3.2.2. Gas-phase CO_2 (≥70 K)

In the remainder of the experiments, listed in Table 1, and shown in Figs. 3, B.3–B.6, the temperature of the ASW ranges from 70 to 120 K. In the temperature range 70–90 K equal amounts of CO are converted into CO_2 as compared to <70 K. However, the majority of the formed CO_2 is immediately released into the gas phase after formation. Similar to Fig. 2, we present the results of ASW at 70 K in Fig. 3. During this experiment ~20% of the formed CO_2 stays on the surface of ASW, while the remainder is released into the gas phase. The release of CO_2 into the gas phase is slightly below the canonical CO_2 desorption temperature, 78 K. This is no surprise as the binding energy of CO_2 bound to H_2O equals 2250 K, while the binding energy between CO_2 molecules is higher at 2415 K (He et al. 2017). During the first hour of VUV irradiation, the ASW surface "traps" some of the formed CO_2 in its deep binding sites, but once these are occupied, most of the subsequently formed CO_2 is released into the gas phase. This is reflected by the initial rapid build up of CO_2 in the infrared during the first VUV irradiation interval (Fig. 3a). Additionally, in Fig. 3c, it is shown that the gas-phase CO_2 builds up during the initial VUV interval, where it reaches steady state at the same time when the growth of solid-state CO_2 levels off. Lastly, during TPD the two main desorption features appear at

approximately 80 and 155 K, but not as prominent as in the 40–60 K experiments. The majority of the CO_2 is released during TPD in the "plateau" region between 85 and 145 K, that is, between the canonical desorption of CO_2 aggregates and H_2O, as is shown in Fig. 3d.

In the experiments with ASW temperatures between 90 and 120 K (Figs. B.4–B.6), no solid-state CO_2 is observed in the infrared (column density $\leq 2.0 \times 10^{13}$ cm^{-2}). The TPDs in this temperature range, however, do reveal that some CO_2 is still bound to the surface of the ASW. Following the trend as seen in the experiments with ASW at 70 and 80 K, the amount of CO_2 that remains on the ASW surface decreases with increasing temperature, see Figs. B.4–B.6. This is in line with the decrease in absolute signal of the "plateau" during TPD. Interestingly, a significant amount of O_2 formation is observed in the 90–120 K temperature range, as shown by the QMS signal at $m/z = 36$ representing $^{18}O_2$. The formation of O_2 increases with temperature at the cost of CO_2. At 120 K, the formation of CO_2 is almost completely quenched. Compared to 80 K the raw QMS data at 120 K for CO_2 is decreased by over a factor of 10 and the O_2 signal increased by over a factor of 50.

3.3. Control experiments

Several control experiments have been performed in order to aid in the investigation of the interaction between gas-phase CO and VUV irradiated water ice. Specifically, a control experiment where a different oxygen isotope is used in CO, an experiment without VUV irradiation, and an experiment where gas-phase CO is omitted, as listed in Table 1. The results of these experiments are presented in Figs. B.7, B.8, and B.9 of Appendix B, respectively.

The experiment with gas-phase $^{13}C^{16}O$, instead of the $^{13}C^{18}O$ isotopologue, provides additional information on the interaction between the gas-phase CO and VUV irradiated water ice (Fig. B.7). In the infrared the three main absorption features are shift by approximately 20 cm^{-1}, 2297, 2280, and 2262 cm^{-1}, with respect to the main experiments, 2279, 2260, and 2243 cm^{-1}, respectively. This indicates that these three CO_2 features are formed through the same process as each of them shift by approximately the same wavenumber due to the difference in mass of the oxygen isotope. Additionally, the QMS results show that the CO_2 is now detected at a m/z that equals 47 ($^{13}C^{16}O^{18}O$) instead of 49 ($^{13}C^{18}O_2$). This indicates that both oxygen atoms from the precursors, that is, ^{16}O from $^{13}C^{16}O$ and ^{18}O from $H_2^{18}O$, are involved in the formation of CO_2.

The experiment without VUV irradiation, shown in Fig. B.8, is performed to track the level of CO_2 from other sources. A build up of 0.1 ML CO_2 is detected during the time that the water ice is exposed to gas-phase CO. Compared to the counterpart experiment with VUV radiation, shown in Fig. 2, this is only 4% of the total CO_2 formed when water ice is VUV irradiated. This small contribution is most likely due to contamination from previous experiments or trace amounts of $^{13}C^{18}O_2$ in our $^{13}C^{18}O$ gas bottle. Regardless, this amount of contamination is negligible.

Lastly, water ice is VUV irradiated without the presence of gas-phase CO in the vacuum chamber. The results of this experiment are presented in Fig. B.9. Both the infrared and the QMS show at most trace amounts of CO_2. This supports that the main processes through which CO_2 in this study is formed through the interaction between gas-phase CO and VUV irradiated water ice. Additionally, the QMS shows the release of O_2 into the gas phase during VUV irradiation, which is not seen in the counterpart main experiment with gas-phase CO, as shown in Fig. 2.
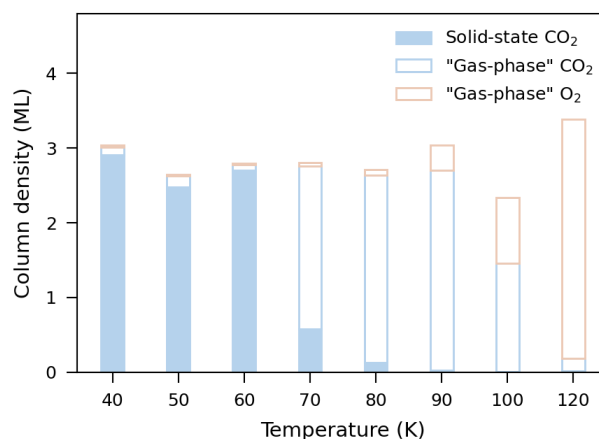

Fig. 4. Column densities of the formed products when ASW is VUV irradiated and exposed to gas-phase CO as function of temperature. Solid-state column densities are derived through RAIRS and gas-phase column densities through the QMS as described in Sect. 2.3. Both the RAIRS and gas-phase data provide information on the gas–surface interactions studied here.

3.4. CO_2 and O_2 column densities

For each of the main experiments the column densities of the products, with a total VUV incident fluence of 4.5×10^{18} photons, are summarized in Fig. 4. The column density of solid-state CO_2 is derived through the combined integrated absorbance area of the three infrared CO_2 features. The CO_2 and O_2 gas-phase column densities are derived through the calibration of the QMS described in Sect. 2.3.2. In short, in the temperature range 40–60 K the main product is solid-state CO_2. As substrate temperatures at 70 K or above, the CO_2 is detected in the gas phase, and at even higher temperatures, that is, ≥ 90 K, O_2 formation is observed at the cost of CO_2 production.

4. Discussion

It is clear from the presented results that CO_2 is formed in our experiments, and that the temperature of the ASW influences the physical appearance of CO_2. In the following section we explore the different pathways to CO_2, which pathway results in the formation of CO_2 in our experiments, and the CO_2 production efficiency per absorbed VUV photon.

4.1. Exploring the reaction network

In the introduction, we mentioned several solid state pathways that can form CO_2. The formation of CO_2 in our experiments is driven by VUV irradiation of ASW that interacts with gas-phase CO. This is different from most earlier studies where CO was embedded and intimately mixed with water ice. Such experiments are relevant for astronomical scenarios in which H_2O and CO are mixed in the solid state. However, these conditions are different from those discussed later in this study, that is, protoplanetary disks (Sect. 5.1) and at molecular cloud edges (Sect. 5.2).

There are two potential pathways to form CO_2 in our experiments, which involve both H_2O and CO, and three possible pathways that could lead to the observed formation of O_2 at higher temperatures. Figure 5 gives a schematic overview of these reactions. In general, UV photons dissociate H_2O in the solid state through its excited $\tilde{A}$ and $\tilde{B}$ states, which mainly lead
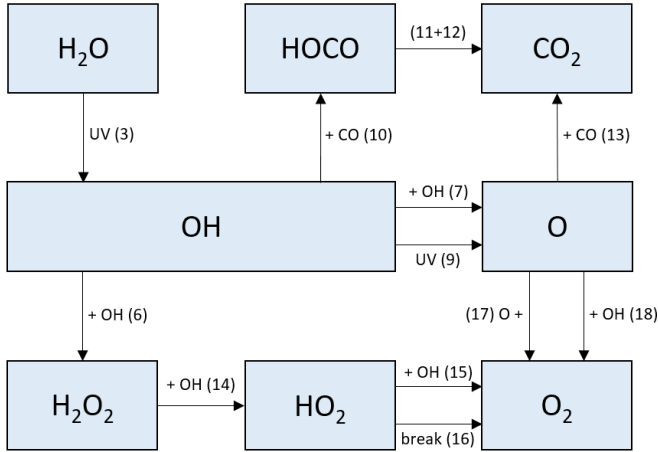
Fig. 5. Schematic overview of the reactions that potentially occur in our experiments with VUV irradiation of solid-state H_2O in the presence of gas-phase CO. The numbers in parenthesis correspond to the reactions in Sect. 4.1. Backward, recombination, and by-products of reactions are not shown for clarity.

to the formation of OH radicals and atomic oxygen,

$$H_2O + h\nu \rightarrow H + OH, \tag{3}$$

$$H_2O + h\nu \rightarrow H_2 + O. \tag{4}$$

Stief et al. (1975) reported quantum efficiencies for both reactions (3) and (4) upon irradiation in two different wavelength ranges, namely 145–185 nm and 105–145 nm corresponding with the excited Ã and B̃ states of solid-state H_2O, respectively. Water dissociated through the excited Ã state has been reported to have quantum efficiencies of 0.99 and ≤0.01 for reactions (3) and (4), respectively. The dissociation through the excited B̃ state was reported to have quantum efficiencies of 0.89 and 0.11, respectively.

In this study, we use a MgF_2 window with a cut-off wavelength above the wavelength of Lyman-α photons. This ensures that Lyman-α photons from the MDHL are absorbed, and that the majority of the UV photons are in the 140–170 nm (7.3–8.9 eV) range, see Fig. A.1. This, combined with the reported quantum efficiencies, results in the dissociation of H_2O only through its excited Ã state, producing mainly OH radicals through reaction (3). The removal of Lyman-α photons makes the VUV spectrum less representative of those in interstellar environments. However, it does allow for an in-depth investigation of primary reactions including only OH radicals.

The formed H and OH proceed in different ways depending on the depth in the ice at which dissociation occurs. The molecular dynamics calculations by Andersson & van Dishoeck (2008) showed that in the top 3 ML the majority of the photodissocation events results in the desorption of H and trapping of OH. At 4 ML or deeper most of the photodissocation events result in trapping of both species or recombination, reforming H_2O through reaction (5),

$$H + OH \rightarrow H_2O. \tag{5}$$

The desorption of H in the top 3 ML results in an enrichment of OH radicals on the surface. It was found in these calculations that the OH radicals can diffuse up to 60 Å on top of the H_2O surface at 10 K. This diffusion occurs on picosecond timescales, and does not include any thermal diffusion on longer

timescales. Hama et al. (2009) showed that the OH radicals produced through reaction (3) are hot and have a translational temperature of 1300 ± 300 K. This significant amount of translational energy allows for additional diffusion, and increases the probability of two OH radicals to meet and react with each other. This reaction either forms hydrogen peroxide (H_2O_2) or H_2O and atomic oxygen, see reactions (6) and (7), respectively. The branching ratio between reactions (6) and (7) was found to be 0.8 and 0.2 for two nonenergetic OH radicals reacting with each other at 40–60 K (Oba et al. 2011),

$$OH + OH \rightarrow H_2O_2, \tag{6}$$

$$OH + OH \rightarrow H_2O + O. \tag{7}$$

As the abundance of the H_2O_2 increases, also the amount of H_2O_2 dissociated by VUV photons increases through reaction (8),

$$H_2O_2 + h\nu \rightarrow OH + OH. \tag{8}$$

The translational temperature of these OH radicals was found to be 7500 ± 1000 K, which potentially allows for even further diffusion of OH radicals across the surface (Hama et al. 2009). These OH radicals on the surface, or those below for that matter, can be subsequently dissociated by VUV photons forming atomic hydrogen and oxygen, see reaction (9),

$$OH + h\nu \rightarrow H + O. \tag{9}$$

The OH radicals formed through reactions (3) and (8) are potential candidates for CO_2 formation when reacting with gas-phase CO. In the experimental study by Oba et al. (2010) the formation of CO_2 was observed from co-deposition of nonenergetic OH radicals, cooled to 100 K prior to deposition, and CO molecules at 10 and 20 K. The authors proposed that CO_2 forms through reactions (10), (11), and (12),
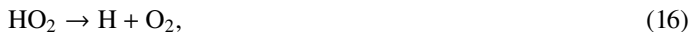
$$CO + OH \rightarrow trans-HOCO, \tag{10}$$

$$trans-HOCO \rightarrow cis-HOCO, \tag{11}$$

$$cis-HOCO \rightarrow CO_2 + H. \tag{12}$$

Atomic oxygen formed through reactions (7) and (9) also has the potential to react with CO and form CO_2 through reaction (13),

$$CO + O \rightarrow CO_2. \tag{13}$$

The addition of atomic oxygen to CO has been experimentally shown to work between 5 and 20 K, where CO is adsorbed on a bare substrate (Roser et al. 2001; Madzunkov et al. 2006; Raut & Baragiola 2011; Ioppolo et al. 2013). The same reaction has also been investigated on top of ASW by Minissale et al. (2013). These authors show that the CO_2 is formed through reaction (13) when CO and O are co-deposited on the surface of ASW in the temperature range 10–50 K.

The initially formed O, OH, and H_2O_2 can react with each other to form the hydroperoxyl radical (HO_2) and O_2. The HO_2 radical is formed through subsequent reactions of H_2O_2 with OH, see reaction (14). Molecular oxygen can be formed through different means, (a) an HO_2 radical reacts with OH, see reaction (15), (b) the HO_2 radical falls apart, see reaction (16), (c) atomic oxygen reacts with another atomic oxygen,

see reaction (17), or (d) atomic oxygen reacts with OH, see reaction (18).

$$H_2O_2 + OH \rightarrow HO_2 + H_2O, \tag{14}$$

$$HO_2 + OH \rightarrow O_2 + H_2O, \tag{15}$$

$$HO_2 \rightarrow H + O_2, \tag{16}$$

$$O + O \rightarrow O_2, \tag{17}$$

$$O + OH \rightarrow O_2 + H. \tag{18}$$

4.2. CO$_2$ formation pathway

In order to disentangle which of the above formation pathways is active in our experiments, we look into the temperature dependence of the CO$_2$ formation process and which isotopes are incorporated in the produced CO$_2$. We also extensively compare with literature data. Across the temperature range of 40–90 K, the total column density of formed CO$_2$ is constant, but above 90 K the efficiency of CO$_2$ formation decreases due to the competing formation of O$_2$, see Fig. 4. This temperature dependence contains significant amount of information, which allows us to constrain the formation of CO$_2$ to one pathway.

Our experiments show that CO$_2$ is formed through the reaction between gas-phase CO and solid-state OH radicals. These OH radicals are the primary product of H$_2$O dissociation, and are thus most likely to react with CO. This particular reaction pathway to CO$_2$ has been investigated extensively (Watanabe & Kouchi 2002b; Watanabe et al. 2007; Ioppolo et al. 2009, 2011; Oba et al. 2010, 2011; Noble et al. 2011; Zins et al. 2011; Yuan et al. 2014). However, the majority of these studies were performed at temperatures where CO is in the solid state, and mixed with H$_2$O. Oba et al. (2010) looked at the formation of CO$_2$ through co-deposition of CO and nonenergetic OH radicals at a temperature of 10 and 20 K. Besides CO$_2$, the authors also observed the intermediate products cis- and trans-HOCO radicals at 1774 and 1812 cm^{-1}, respectively. They found that the HOCO absorption features disappear at $T > 40$ K, which is in line with the experimental work of Milligan & Jacox (1971). This is most likely the reason why the cis- and trans-HOCO radicals are not detected in the infrared spectra of our experiments (spectra not shown). In a follow-up study, Oba et al. (2011) investigated the same reactions, but in the temperature range 40–60 K. Formation of CO$_2$ was observed in the infrared, but the efficiency at which CO was converted into CO$_2$ decreased with increasing temperature. The conversion rates were found to be 1.4%, 0.8%, and 0.3% at 40, 50, and 60 K, respectively. This decrease was attributed to the decreasing residence times with increasing surface temperature of both CO and OH. In our experiments this efficiency decrease is not observed, even when only considering solid-state CO$_2$. A possible explanation for this is the different origin of the OH radicals; in our work the radicals are formed in situ with excess energy, whereas in previous studies OH radicals were deposited.

The other proposed formation pathway to CO$_2$, that is, atomic oxygen reacting with CO, can be excluded. This is because atomic oxygen can only originate in our experiments as a secondary product through reactions (7) and (9). Additionally, on ASW atomic oxygen and CO have similar binding energies, that is, 1320 and 1350 K, respectively, and thus their residence times on the surface are comparable (Minissale et al. 2016;

He et al. 2016a). Because of their similar residence times, no difference should be observed between the formation of CO$_2$ and O$_2$ with experimental temperature. However, O$_2$ is only significantly formed at temperatures ≥ 90 K. This is proof that atomic oxygen is not involved in the formation of CO$_2$. Lastly, Minissale et al. (2013) investigated the formation of CO$_2$ through co-deposition of CO and atomic oxygen on top of ASW. It was found that the efficiency of CO$_2$ formation peaked at 35 K and dropped to zero at 60 K. As CO$_2$ formation is observed in our experiments up to 120 K, this is again evidence that atomic oxygen is not involved in the formation of CO$_2$ in our experiments. It should be noted that experimental conditions are not identical, as in our experiments the atomic oxygen would be formed in situ instead of co-deposited with CO. However, since atomic oxygen would be in the ground state, for both our work and that of Minissale et al. (2013), no clear differences are expected.

Formation of CO$_2$ through excited CO* reacting with another CO molecule on the surface of ASW can also be ruled out. This is unlikely to occur, because it would require a CO molecule to be excited during its short, but nonzero, residence time and react with another CO molecule which has an equally short residence time. Additionally, in the control experiment with H$_2^{18}$O and ^{13}C^{16}O, the formed CO$_2$ is measured with the QMS during TPD at $m/z = 47$, corresponding to ^{13}C^{16}O^{18}O, see Appendix B.7. If the CO$_2$ would be formed through excited CO and another CO molecule it would be expected to be detected at $m/z = 45$, corresponding to ^{13}C^{16}O$_2$.

From above results and discussion it is most likely that CO$_2$ is formed through the interaction between CO and OH radicals, formed by UV dissociation of H$_2$O. However, it is not yet clear if CO directly interacts with OH radicals from the gas phase, that is, an Eley–Rideal type reaction, or if CO adsorbs onto the ASW, diffuses, and subsequently reacts with OH radicals, that is, a Langmuir-Hinshelwood type reaction. Additionally, the formation location of CO$_2$ is also not yet clear; is it formed on the surface or embedded in the ASW? Both of these topics are discussed in the following section.

4.3. Formation location of CO$_2$

The average time a species resides on a surface can be estimated at a given temperature starting from the measured or calculated binding energy to that surface. We derive that CO has residence times on ASW of 4.5×10^2–7.7×10^{-8} s in the range from 40 to 120 K. This is found through the Arrhenius equation, which can be written as

$$k = A e^{-\frac{E_{\text{bind}}}{T}}, \tag{19}$$

where k is the rate constant, A the frequency factor, which is taken to be 10^{12} s^{-1}, E_{bind} the binding energy of a species to a specific surface in K, and T the temperature of the surface in K. The residence time is then given by the reciprocal of the rate constant from Eq. (19). For CO on ASW, the binding energy is dependent on the CO surface coverage, ranging from 1000 to 1700 K at 1–10^{-3} ML coverage (He et al. 2016a). The above residence times are estimated given an average binding energy of 1350 K for CO on ASW. For comparison, the binding energy of CO on the CO–CO interface is 855 ± 25 K (Öberg et al. 2005).

Even within these short residence times, some diffusion across the surface is expected. The number of binding sites CO visits on ASW, before desorption occurs, is estimated to be 7.2×10^{10}–4.2×10^3 in the range 40–120 K. This is also derived through Eq. (19). Specifically, the number of different binding

sites a molecule can visit before a species desorbs is approximated by dividing the diffusion rate by the desorption rate. The diffusion rate is estimated by exchanging the E_{bind} term in Eq. (19) for the diffusion energy (E_{diff}). The rate constant is then a proxy of the number of hops a species makes between different binding sites per second. The diffusion energy for CO on ASW has recently been measured in situ with transmission electron microscopy (TEM), and was found to be 350 ± 50 K (Kouchi et al. 2020).

Given these residence times and amount of binding sites that are "visited" before desorption occurs, we conclude that CO spends sufficient time on the surface of ASW to react with OH radicals through a Langmuir-Hinshelwood type reaction. This is different from Yuan et al. (2014), who investigated this reaction under similar experimental conditions and attributed it to an Eley–Rideal type of reaction. Yuan et al. (2014) employed a slightly higher binding energy of 0.125 eV (1450 K) for CO on H_2O, which results in a residence time of $\sim 2 \times 10^{-4}$ s at their experimental temperature of 76 K. The residence time is used to calculate the fractional coverage of CO on H_2O and was found to be 1×10^{-6} ML. The resulting fractional coverage of OH was derived to be 0.05 ML, over four orders of magnitude higher, which led to the conclusion of an Eley–Rideal type of reaction. However, diffusion of CO during this (short) residence time was not considered. At these temperatures, CO visits approximately 10^6 binding sites during its residence time, and thus, the effective surface scanned by CO is ~ 1 ML even though the fractional coverage of CO is only 1×10^{-6} ML. This supports that the involved mechanism follows a Langmuir-Hinshelwood type reaction.

Furthermore, we see no evidence of significant CO diffusion, and subsequent trapping, into the bulk of the H_2O ice. However, there is some trapping of CO on the surface or pores of the ASW. This is shown in a control experiment where ASW is exposed to CO molecules, but not to VUV irradiation. During TPD of this control experiment, as is shown in Appendix B.8, the majority of the CO desorbs at approximately 50 K. Only a small amount of CO "volcano" desorbs when the ASW crystallizes. It is most likely that this CO got trapped in ASW due to pore collapse, instead of actually diffusing into the bulk ASW.

4.4. Temperature dependent formation, CO_2 vs. O_2

At ASW temperatures above 90 K, the production of O_2 increases at the cost of CO_2 formation (see e.g., Fig. 4). An in-depth investigation of O_2 formation is beyond the scope of this work, but it is briefly discussed to explain the decrease in CO_2 production. For more information on O_2 production, we refer to a recent study that quantitatively investigated the production of O_2 and H_2O_2 by VUV irradiation of H_2O (Bulak et al. 2022).

Since O_2 formation occurs at the cost of CO_2 production, it is likely that both species have a common precursor. In Sect. 4.1, the pathways to O_2 are through the OH radical or atomic oxygen. Due to the high temperature and simultaneous increase and decrease in O_2 and CO_2 abundance, respectively, the O_2 is likely formed through OH radicals. These OH radicals form O_2 sequentially through H_2O_2 and HO_2, see reactions (14), (15), and (16). The formation of O_2 involving atomic oxygen is unlikely, as it is shown to not be involved in the formation of CO_2, see Sect. 4.2. Additionally, in our experiments atomic oxygen is a secondary product through reactions (7) and (9). The low residence times of this atomic oxygen, $<2.3 \times 10^{-6}$ s at temperatures above 90 K, combined with low availability makes formation of O_2 through OH radicals the dominant pathway.

The formation of CO_2 and O_2 is dependent on the availability of OH radicals and the temperature of the ASW. Given this temperature dependence, it is likely that the increased mobility of the OH radical and reduced residence time of CO at high temperatures holds the answer to why O_2 formation is more favourable. The pathway to form O_2 at high temperatures is worthy of further investigation.

4.5. Conversion rate of CO into CO_2

In order to demonstrate that the gas-grain pathway to convert CO into CO_2 is a process of importance in astrophysical environments, we discuss in this section the conversion rate and limiting factors in our experiments. In total, ~ 60 ML of water ice are deposited on the substrate in preparation of our experiments. However, as this conversion of CO into CO_2 occurs on the surface, not all of this H_2O is available to act as a reacting medium. Classically, the surface of solid-state H_2O contains approximately 10^{15} molecules per cm^2. However, due to the porous nature of our ASW, the available H_2O surface for CO to adsorb on is expected to be larger. Additionally, with hydrogen released from the top three monolayers upon UV dissociation of H_2O, and the mobility of the OH radicals, we assume that OH radicals formed in the top three monolayers are available to convert CO into CO_2 (Andersson & van Dishoeck 2008). These top three monolayers, that is, 3.0×10^{15} H_2O molecules cm^{-2}, are henceforth the reactive surface.

The VUV radiation that impacts the water ice, consists only of photons from molecular H_2 emission, as the Lyman-α photons of the MDHL are absorbed by our MgF_2 window, see Fig. A.1. The average H_2O absorption cross section for the VUV photons is taken to be $(1.2 \pm 0.1) \times 10^{-18}$ cm^2. This average is derived from the absorption cross section of the two main molecular H_2 emission peaks at 157.8 and 160.8 nm in a one-to-one ratio (Cruz-Diaz et al. 2014). Given this cross section and the Beer-Lambert law, $\sim 0.4\%$ of the total incident VUV fluence is absorbed by H_2O in the reactive surface, and this equals 1.6×10^{16} photons. On the assumption that H_2O dissociation is 100% efficient, this produces an equal amount of OH radicals in the reactive surface. In the temperature range 40–90 K, approximately 2.7×10^{15} CO_2 molecules are formed, and thus an equal amount of OH radicals is consumed through reactions (10)–(12). This means that, for the above assumption, only 17% of the available 1.6×10^{16} OH radicals are involved in the conversion of CO into CO_2. The question is, what is the limiting factor that determines this efficiency factor?

In our experiments, it is the amount of OH and not CO that is limiting the formation of CO_2. In the temperature range of 40–90 K, the formation of CO_2 is considered to be constant. However, the residence time of CO is lowered by a factor of 10^8 and the binding sites visited by CO by a factor of 10^5 from 40 to 90 K. That is to say, once CO finds an OH radical on the surface that is available, the conversion into CO_2 is (close to) unity. The relatively small fraction (17%) of VUV absorption events resulting in the CO_2 production may be due to a smaller number of available OH radicals, for example, the recombination probability of H + OH on the surface is high. It is also possible that other products are formed besides CO_2 or that UV dissociation of ASW is not unity, which is typically assumed. These are in our view the most logical explanations. Below we argue why from these options the dissociation efficiency of solid-state H_2O is most likely the limiting factor in the formation of CO_2.

It would be surprising if a significant portion of the available OH radicals would not react, because even nonenergetic OH

radicals in the ground state are able to form CO_2 with CO at 10 K (Oba et al. 2010). Formation of other products, such as, H_2O_2, is also excluded as we do not detect significant amounts of the possible products in the experiments. Assuming that VUV photodissociation of water ice is unity and recombination does not occur in the reactive surface, the reactive surface would be dominated by OH radicals (83% of the remaining VUV absorption events). This amount of OH radicals should largely find each other and react to form H_2O_2 and O_2. The infrared does not show any of the vibrational modes of H_2O_2 within our detection limits (spectra not shown), especially not with the expected H_2O_2 column density of ∼7 ML, assuming that all of the remaining OH radicals react with each other and form H_2O_2 through reaction (6). In itself this column density is already questionable, as it is approximately twice the amount of available H_2O molecules in the reactive surface. Additionally, a control experiment where ASW is irradiated at 40 K and gas-phase CO is omitted does show the formation of H_2O_2 and O_2, see Appendix B.9. This shows that in the presence of gas-phase CO the formation of H_2O_2 and O_2 in the reactive surface is quenched, and that in the main experiments all available OH radicals react with CO into CO_2.

The amount of CO_2 produced, and lack of other products, in the experiments points at that either the recombination of H + OH is high in the reactive surface or that not every VUV absorption event results in the dissociation of H_2O. Fully investigating this question is beyond the scope of this work, but it leads to a conundrum that requires attention. It is unlikely that recombination to H_2O is significantly more efficient than predicted by molecular dynamics calculations. Photodissociation and desorption occur on picosecond timescales after VUV absorption in these simulations, and thus, diffusion of atomic hydrogen within this time window is improbable. It should be noted that in molecular dynamics calculations only a single event is considered per simulation, and thus for H_2O recombination to occur the atomic hydrogen needs to find its original OH partner before it desorbs. It could be that in our experiments the atomic hydrogen reforms H_2O with previously formed OH radicals due to the high VUV photon fluxes, that is, 2.5×10^{14} photons s^{-1} cm^{-2}. Molecular dynamics calculations of H_2O photodissociation and recombination with neighbouring available OH radicals are needed to test if this pathway is viable. For now we deem it inefficient due to the extremely short time scales in which desorption occurs after dissociation.

A lower dissociation efficiency of water ice upon absorption of a VUV photon, that is, well below unity, seems to be the most likely explanation for our findings, at least based on the processes discussed here. In Fig. 2 of Andersson & van Dishoeck (2008) the fractional probabilities of photodissociation pathways for H_2O are given per absorbed photon and sum to (near) unity. However, per design these simulations only follow H_2O that is photodissociated. Schriever et al. (1990) investigated the absolute photodissociation quantum yield of H_2O in an argon matrix (ratio 1:500). It was found that at 160 nm and 5 K the photodissociation efficiency of isolated H_2O in argon equals 20–30%. It should be noted that in their work the H_2O is isolated and trapped in the bulk argon, which cannot be extrapolated to our work. That being said, it does match well with our 17% efficiency, which suggests that indeed the dissociation of water ice, through the excited Ã state, is not unity. Similar results have been found by Kalvāns (2018) who investigated how the photodissociation efficiency differs in general for a molecule in the gas-phase and solid-state. They found a best-fit value of 0.3 for the ratio solid-state to gas-phase photodissociation from their 1D astrochemical

model in comparison to line-of-sight observations of collapsing interstellar clouds. Even though our findings are not fully conclusive, it seems to be in line with results presented earlier in the literature.

Arasa et al. (2013) investigated the CO + OH pathway at 10 K with molecular dynamics calculations and found a conversion probability for CO_2 of $(3.6 \pm 0.7) \times 10^{-4}$ per absorbed photon, which is significantly lower than our 17%. However, it was found that the formation probability of the intermediate HOCO complex is two orders of magnitude higher with $(3.00 \pm 0.07) \times 10^{-2}$ per absorbed photon. This is explained by the HOCO complex being trapped in the solid state and losing its internal energy to the surrounding molecules, which prevents further reaction to CO_2 + H. This does not necessarily align with the findings presented here. In our experiments the HOCO complex is not observed. However, it could very well be that this HOCO complex is briefly present, but transfers into CO_2 due to the increased ASW temperature, as seen in Milligan & Jacox (1971) and Oba et al. (2011). Even then our formation efficiency is significantly higher than their calculated efficiency, which even includes an assumed solid-state dissociation efficiency of unity. We postulate that this is because of the difference in temperature and that the calculations only consider isolated events, while in the work described here many CO molecules and OH radicals are present at once, which could increase reaction probabilities.

A possible source of error in our determination of the formation efficiency are the experimental assumptions. Using Gaussian error propagation, we estimate the error in our formation efficiency of CO_2 per absorbed VUV photon in the reactive surface to be 60%, and thus ranges from 7 to 27%. Errors include, but are not limited to, assumptions made on the area which the infrared probes, the apparent band strength of $^{13}C^{18}O_2$, and the RAIRS correction factor. Although the propagation of all the individual errors results in a large uncertainty on our derived efficiency it is still at least four times smaller than the generally assumed value of unity for UV dissociation of water ice.

5. Astrophysical implications

Figure 6 schematically summarizes the above results and discussion. The formation of CO_2 through interaction between gas-phase CO and VUV induced OH radicals on water ice is visualized in the top row of this figure. Details on this process are discussed in Sect. 4. In short, CO has a short, but nonzero, residence time on water ice even though its temperature is above the canonical sublimation temperature of CO. Concurrently, the water ice is irradiated with VUV photons, which results in the production of OH radicals. The diffusion of CO and OH radicals across the surface allows them to react with each other and form CO_2 in a Langmuir-Hinshelwood type reaction. Depending on the temperature of the water ice, the CO_2 is either mainly bound to the water ice, forms aggregates on top of the water ice, or is released into the gas phase, as is shown in the bottom row of Fig. 6. A full analysis of the experiments is given in Sect. 3, but briefly, in the lower end of the experimental temperature range, that is, 40–60 K, the formed CO_2 remains in the solid state. Specifically, at 40 K (Fig. 6e) the CO_2 is not mobile enough and the majority of the CO_2 stays bound to the ASW surface. However, in the experiment at 60 K (Fig. 6f), the CO_2 has significant mobility and starts diffusing across the surface, and forms CO_2 aggregates on top of the ASW. As shown in Fig. 6g, the formed CO_2 is released into the gas phase at 80 K, and at higher temperatures, the formation of O_2 starts competing with CO_2, which is
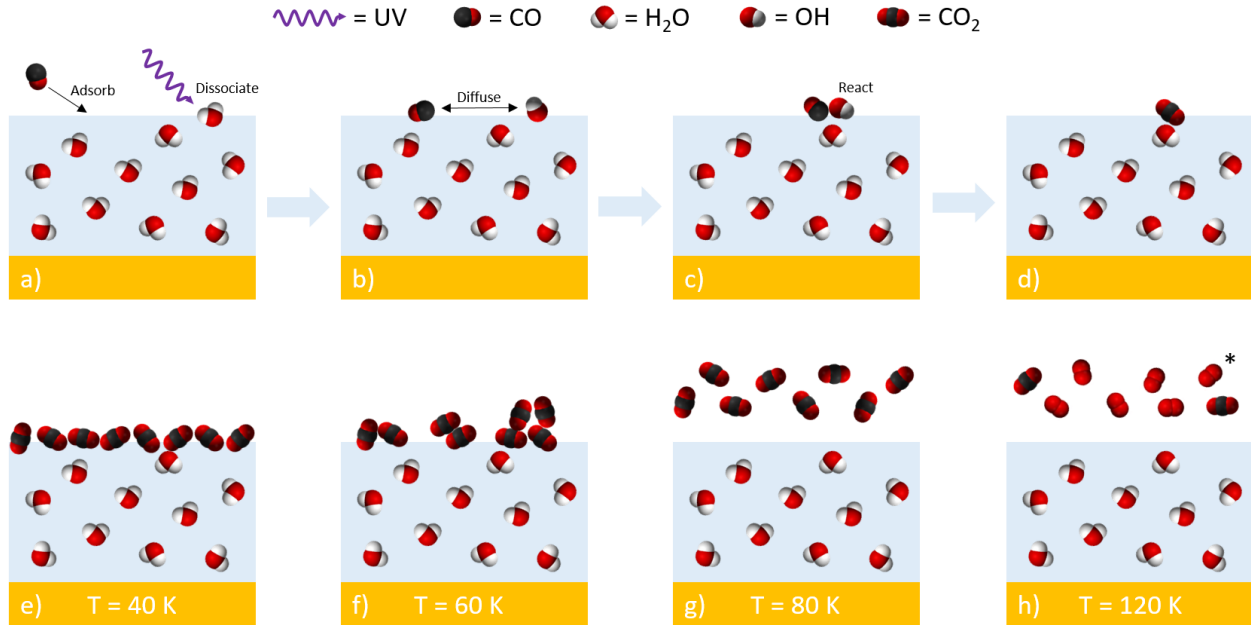
Fig. 6. Simplistic representation of the processes that occur in our experiments. *Panel a–d* show the proposed Langmuir–Hinshelwood reaction that creates CO_2 in our experiments. Panels in the bottom row schematically show the structure or phase in which the formed products end up after formation, given a certain experimental temperature. [*]Molecular oxygen is not formed through the depicted reaction, for details see Sects. 4.1 and 4.4.

shown in Fig. 6h. In the 40–90 K range, our experiments show that 7–27% of the absorbed UV photons in the reactive surface, that is, top three monolayers of ASW, result in the conversion of gas-phase CO into CO_2. In the following section, we look at two astrophysical environments, that is, protoplanetary disks and molecular clouds, where this pathway could play an important role and may explain observational findings.

5.1. CO conversion in protoplanetary disks

In planet forming disks, the gas mass, as derived through CO isotopologues, often comes out factors 10–100 lower than expected based on the dust content. This finding is based on physical–chemical that includes photodissociation and freeze out of CO and its isotopologues or thermo-chemical modeling (Miotello et al. 2014, 2016, 2017; Calahan et al. 2021). One interpretation is that these disks have already lost a significant fraction of their total gas mass. Another is that some unknown process locks up gas-phase CO on grains. A correct interpretation is essential for models of planet formation that rely on the available gas-mass reservoir as well as on the gas-to-dust ratio. Other gas-mass tracers are problematic, as H_2 is undetectable and HD has only been observed in a few sources (see e.g., Bergin et al. 2013; McClure et al. 2016; Trapman et al. 2017; Kama et al. 2020), where, incidentally, the HD data support the notion of gas-phase CO being locked up. The CO into CO_2 conversion has been proposed as a possible pathway to convert gas-phase CO into a species that is much more difficult to detect.

Chemical models by Bosman et al. (2018) looked at several pathways through which CO could be converted into less volatile species to explain the low observed CO fluxes. These models are successful in this conversion on timescales shorter than average protoplanetary disk lifetimes, that is, ~3 Myr. It should be noted that it was found in these models that gas-phase CO is in competition with atomic hydrogen for OH radicals on the surface (see Bosman et al. 2018, for more details). Furthermore, these results depend on the adopted binding energies, reaction rates,

and formation of H_2. For example, the binding energy of CO in these models is kept constant at 855 K, no matter the environment. However, it has been found that the binding energy of CO on ASW can be as high as 1700 K (He et al. 2016a). In a similar fashion, Trapman et al. (2021) used physical–chemical models to investigate the low CO fluxes in the Lupus star-forming region. Disk regions with $T_{gas} > 35$ K were excluded in these models for gas-phase CO conversion, as verification models showed that CO conversion through grain-surface chemistry is negligible at these temperatures, but again this was tested with a CO binding energy of 855 K.

Including the correct binding energy for CO on ASW in these types of models is crucial. This increased binding energy allows gas-phase CO to compete with atomic hydrogen for OH radicals in a larger temperature range, and thus a larger region in protoplanetary disks where CO can be removed from the gas phase. In our experiments, the models by Bosman et al. (2018), and Trapman et al. (2021), the amount of gas-phase CO that is converted into CO_2 depends on the availability of OH radicals. The authors assume in their models that once H_2O absorbs a VUV photon, dissociation is 100% efficient. As discussed in Sect. 4.5, our experiments show an efficiency for OH production of 7–27% per absorbed UV photon as opposed to the 100% adopted in the models. Further modeling is required, which also includes the correct binding energy of CO on ASW, to fully assess the impact of our results on the model predictions about the consumption of gas-phase CO through this gas-grain interaction.

5.2. CO₂ formation in edges of molecular clouds

Observations of icy grains surrounding young stars suggest that large amounts of the observed solid-state CO_2 is in a water-rich environment (see e.g., Boogert et al. 2015). Here, we explore if the conversion of gas-phase CO into solid-state CO_2 investigated in this work could (partially) explain the presence of solid-state CO_2 embedded in water ice (Pontoppidan et al. 2008).

It is generally assumed that the ice that covers dust grains is composed of two layers: a polar and an apolar layer, where the apolar layer is formed on top of the polar layer. The polar ice layer is dominated by species with larger dipole moments, such as H_2O, and the apolar ice layer mainly contains species with smaller or no dipole moments, such as CO and N_2. Over the years solid-state CO_2 has been detected in a large number of sources. For example, Gerakines et al. (1999) observed solid-state CO_2 with ISO in molecular clouds in a range of different physical environments. Their analysis shows that the majority of the observed solid-state CO_2 is found in a polar environment. Additionally, the *Spitzer* "Cores to Disks" program similarly showed that in embedded young low-mass stars the majority of the observed solid-state CO_2 is mixed in a polar water-rich environment (Pontoppidan et al. 2008). Given these H_2O-dominated environments, it is possible that a substantial fraction of this CO_2 is formed through reactions between CO and OH radicals. This would require CO to freeze out during H_2O formation in order to be intimately mixed and subsequently to be converted into CO_2.

Infrared observations show that it is unlikely that CO is mixed in a water-rich environment. The observed CO absorption feature can be deconvolved into three components, namely 4.665 μm (2143.7 cm^{-1}), 4.673 μm (2139.7 cm^{-1}), and 4.681 μm (2136.5 cm^{-1}). The blue component (4.665 μm) is assigned to CO in an apolar environment, specifically, it is linked to mixtures of solid-state CO and CO_2 (Boogert et al. 2002; van Broekhuizen et al. 2006) or crystalline CO (Pontoppidan et al. 2003). The middle component (4.673 μm) is generally attributed to pure CO (see e.g., Boogert et al. 2002). The red component (4.681 μm) has a broader "footprint" compared to the other two and is linked to CO in a polar environment. This polar environment could be H_2O and would set the scene for solid-state formation of CO_2 in a polar environment. However, Sandford et al. (1988) showed that if CO would reside in H_2O, one can expect a feature at 4.647 μm (2151.9 cm^{-1}) due to the dangling OH bond, which has not been seen in interstellar spectra. It is thus unlikely that this CO is mixed with H_2O. Mixtures of CO with CH_3OH, however, do reproduce the red component in both peak position and width (Cuppen et al. 2011). A mixture of CO and CH_3OH is also more likely, as CH_3OH is formed through hydrogenation of CO (Hiraoka et al. 1994, 2002; Watanabe & Kouchi 2002a; Hidaka et al. 2004; Watanabe et al. 2004; Fuchs et al. 2009; Santos et al. 2022).

In order to explain the solid-state CO_2 embedded in water-rich environments without invoking the need for CO embedded in H_2O ice, we look at the initial build-up of water ice on dust grains. Water can be formed through both gas-phase and solid-state pathways. However, the gas-phase ion-molecule chemistry produces only a fraction of the total observed water abundance, and thus water is mainly formed through the addition of hydrogen to atomic oxygen on the surface of dust grains (see reviews by van Dishoeck et al. 2014; Linnartz et al. 2015, and references therein). This formation process of solid-state H_2O takes place in the edges of molecular clouds at intermediate extinction (A_V). At this extinction, CO is already present, but still resides in the gas phase. For example, in the Taurus molecular cloud water ice is detected at a threshold extinction, that is, the extinction at which a species is detected in the solid state, of $3.2 \pm 0.1 \, A_V$, while for CO the threshold extinction was determined to be $6.7 \pm 1.6 \, A_V$ (Whittet et al. 2001, 2010). Physical-chemical models of molecular clouds show that the dust–grain temperature at the edge of a cloud equals 31 K, with an external VUV field strength of 100 G_0, where G_0 is a scaling factor in multiples of the average local interstellar radiation field (Habing 1968), which indeed is

sufficient to keep CO in the gas phase (Hollenbach et al. 2009). For CO_2 to be mixed with H_2O it has to form simultaneously, and since CO is in the gas-phase during H_2O formation, CO_2 can be formed through the process described in this work. The OH radicals required for the conversion of CO into CO_2 are readily available in this region. They are the intermediate product to H_2O formation, and the external UV field is still sufficient at this extinction to photodissociate already existing H_2O molecules.

The solid-state CO_2 that is observed to be embedded in water-rich environment in the "Cores to Disks" program, has a relative average abundance w.r.t. H_2O of ~0.2. Assuming that roughly equal amounts of atomic oxygen go into CO and H_2O, this would imply that approximately 20% of the gas-phase CO would have to be converted into solid-state CO_2 to explain observed abundances. Inclusion of this pathway in physical–chemical models of molecular clouds is required to test how efficient this process is in low-density regions at interstellar timescales and explain the observed solid-state CO_2 abundances.

6. Conclusions

The work presented is principally different from many other solid-state astrochemical experiments presented in the past, as it implicitly takes into account gas-grain interactions. A number of systematic measurements have been performed in the temperature range of 40–120 K. Control experiments are performed to narrow down the possible interpretations of the results. Our findings are summarized as follows:

1. The interaction between gas-phase CO and vacuum-UV irradiated water ice produces CO_2 up to 120 K. Solid-state CO_2 is observed in the temperature range 40–60 K. At 70 K or above, the formed CO_2 is released into the gas phase. Additionally, above 90 K the formation of O_2 is observed at the cost of CO_2 production;

2. The residence time of CO on water ice is significant, even though it is above the canonical sublimation temperature of CO. In this short, but nonzero, residence time, a CO molecule is able to diffuse up to 7.2×10^{10} different binding sites before desorption occurs. This significant diffusion allows CO to find an OH radical, created by VUV dissociation of H_2O, and form CO_2 in a Langmuir-Hinshelwood type reaction;

3. Given that gas-phase CO can only interact with the surface of the water ice, this includes pores exposed to the vacuum, we derived a conversion efficiency of 7–27% per absorbed photon in the reactive surface (i.e., top three monolayers). The limiting factor in this conversion rate is the production of OH radicals;

4. The VUV dissociation efficiency of solid-state H_2O is likely the limiting factor in the above conversion efficiency from gas-phase CO into CO_2.

5. Understanding this process is important for astrophysical regions, such as planet-forming disks and molecular clouds. In clouds, this process can explain the presence of solid-state CO_2 embedded in water-rich ices. In disks, it has been invoked to explain the lack of gas-phase CO. Our results suggest that the process might be more complex than those incorporated in the physical–chemical models. Further theoretical investigation is required to investigate the conversion of gas-phase CO into CO_2 to its full extent.

This work demonstrates the wide temperature efficacy of this gas-grain interaction process. Future work, should focus on further experimental and theoretical exploration of the molecular

dynamics which include the effects of high fluxes and neighbouring OH radicals on the reforming of H_2O after photodissociation. Additionally, these results should be included quantitatively in models of planet-forming disks and molecular clouds. With this work we show that gas and grain chemistry cannot be considered as fully separate, but that, under the right conditions, interaction of the gas with the icy surface results in observable effects. It is interesting to realize, that similar processes might also at play for other gas-phase molecules that interact with icy grains.

References

Andersson, S., & van Dishoeck, E. F. 2008, A&A, 491, 907
Ansdell, M., Williams, J. P., van der Marel, N., et al. 2016, ApJ, 828, 46
Arasa, C., van Hemert, M. C., van Dishoeck, E. F., & Kroes, G. J. 2013, J. Phys. Chem. A, 117, 7064
Bennett, C. J., Jamieson, C. S., & Kaiser, R. I. 2009, Phys. Chem. Chem. Phys. (Incorp. Faraday Trans.), 11, 4210
Bergin, E. A., Cleeves, L. I., Gorti, U., et al. 2013, Nature, 493, 644
Boogert, A. C. A., Hogerheijde, M. R., & Blake, G. A. 2002, ApJ, 568, 761
Boogert, A. C. A., Gerakines, P. A., & Whittet, D. C. B. 2015, ARA&A, 53, 541
Bosman, A. D., Walsh, C., & van Dishoeck, E. F. 2018, A&A, 618, A182
Bouilloud, M., Fray, N., Bénilan, Y., et al. 2015, MNRAS, 451, 2145
Bulak, M., Paardekooper, D. M., Fedoseev, G., et al. 2022, A&A, 657, A120
Calahan, J. K., Bergin, E., Zhang, K., et al. 2021, ApJ, 908, 8
Cruz-Diaz, G. A., Muñoz Caro, G. M., Chen, Y. J., & Yih, T. S. 2014, A&A, 562, A119
Cuppen, H. M., Penteado, E. M., Isokoski, K., van der Marel, N., & Linnartz, H. 2011, MNRAS, 417, 2809
Drozdovskaya, M. N., Walsh, C., van Dishoeck, E. F., et al. 2016, MNRAS, 462, 977
Eistrup, C., Walsh, C., & van Dishoeck, E. F. 2016, A&A, 595, A83
Fayolle, E. C., Bertin, M., Romanzin, C., et al. 2011, ApJ, 739, L36
Fayolle, E. C., Bertin, M., Romanzin, C., et al. 2013, A&A, 556, A122
Fillion, J.-H., Fayolle, E. C., Michaut, X., et al. 2014, Faraday Discuss., 168, 533
Fuchs, G. W., Cuppen, H. M., Ioppolo, S., et al. 2009, A&A, 505, 629
Fulvio, D., Raut, U., & Baragiola, R. A. 2012, ApJ, 752, L33
Gerakines, P. A., Schutte, W. A., & Ehrenfreund, P. 1996, A&A, 312, 289
Gerakines, P. A., Whittet, D. C. B., Ehrenfreund, P., et al. 1999, ApJ, 522, 357
Goumans, T. P. M., & Andersson, S. 2010, MNRAS, 406, 2213
Goumans, T. P. M., Uppal, M. A., & Brown, W. A. 2008, MNRAS, 384, 1158
Habing, H. J. 1968, Bull. Astron. Inst. Netherlands, 19, 421
Hama, T., Yabushita, A., Yokoyama, M., Kawasaki, M., & Andersson, S. 2009, J. Chem. Phys., 131, 054508
He, J., Acharyya, K., & Vidali, G. 2016a, ApJ, 825, 89
He, J., Acharyya, K., & Vidali, G. 2016b, ApJ, 823, 56
He, J., Emtiaz, S. M., & Vidali, G. 2017, ApJ, 837, 65
Hidaka, H., Watanabe, N., Shiraki, T., Nagaoka, A., & Kouchi, A. 2004, ApJ, 614, 1124
Hiraoka, K., Ohashi, N., Kihara, Y., et al. 1994, Chem. Phys. Lett., 229, 408
Hiraoka, K., Sato, T., Sato, S., et al. 2002, ApJ, 577, 265
Hollenbach, D., Kaufman, M. J., Bergin, E. A., & Melnick, G. J. 2009, ApJ, 690, 1497
Ioppolo, S., Palumbo, M. E., Baratta, G. A., & Mennella, V. 2009, A&A, 493, 1017
Ioppolo, S., van Boheemen, Y., Cuppen, H. M., van Dishoeck, E. F., & Linnartz, H. 2011, MNRAS, 413, 2281
Ioppolo, S., Fedoseev, G., Lamberts, T., Romanzin, C., & Linnartz, H. 2013, Rev. Sci. Instrum., 84, 073112

Jamieson, C. S., Mebel, A. M., & Kaiser, R. I. 2006, ApJS, 163, 184
Kalvāns, J. 2018, MNRAS, 478, 2753
Kama, M., Trapman, L., Fedele, D., et al. 2020, A&A, 634, A88
Kim, Y.-K., Irikura, K., Rudd, M., et al. 2004, Electron-Impact Ionization Cross Section for Ionization and Excitation Database (version 3.0)
Kouchi, A., Furuya, K., Hama, T., et al. 2020, ApJ, 891, L22
Lehmann, B., Wahlen, M., Zumbrunn, R., Oeschger, H., & Schnell, W. 1977, Appl. Phys., 13, 153
Ligterink, N. F. W., Coutens, A., Kofman, V., et al. 2017, MNRAS, 469, 2219
Ligterink, N. F. W., Terwisscha van Scheltinga, J., Taquet, V., et al. 2018a, MNRAS, 480, 3628
Ligterink, N. F. W., Walsh, C., Bhuin, R. G., et al. 2018b, A&A, 612, A88
Linnartz, H., Ioppolo, S., & Fedoseev, G. 2015, Int. Rev. Phys. Chem., 2015, 34, 205
Loeffler, M. J., Baratta, G. A., Palumbo, M. E., Strazzulla, G., & Baragiola, R. A. 2005, A&A, 435, 587
Madzunkov, S., Shortt, B. J., Macaskill, J. A., Darrach, M. R., & Chutjian, A. 2006, Phys. Rev. A, 73, 020901
Martín-Doménech, R., Manzano-Santamaría, J., Muñoz Caro, G. M., et al. 2015, A&A, 584, A14
McClure, M. K., Bergin, E. A., Cleeves, L. I., et al. 2016, ApJ, 831, 167
Mennella, V., Baratta, G. A., Palumbo, M. E., & Bergin, E. A. 2006, ApJ, 643, 923
Milligan, D. E., & Jacox, M. E. 1971, J. Chem. Phys., 54, 927
Minissale, M., Congiu, E., Manicò, G., Pirronello, V., & Dulieu, F. 2013, A&A, 559, A49
Minissale, M., Loison, J. C., Baouche, S., et al. 2015, A&A, 577, A2
Minissale, M., Congiu, E., & Dulieu, F. 2016, A&A, 585, A146
Miotello, A., Bruderer, S., & van Dishoeck, E. F. 2014, A&A, 572, A96
Miotello, A., van Dishoeck, E. F., Kama, M., & Bruderer, S. 2016, A&A, 594, A85
Miotello, A., van Dishoeck, E. F., Williams, J. P., et al. 2017, A&A, 599, A113
Noble, J. A., Dulieu, F., Congiu, E., & Fraser, H. J. 2011, ApJ, 735, 121
Oba, Y., Watanabe, N., Kouchi, A., Hama, T., & Pirronello, V. 2010, ApJ, 712, L174
Oba, Y., Watanabe, N., Kouchi, A., Hama, T., & Pirronello, V. 2011, Phys. Chem. Chem. Phys. (Incorp. Faraday Trans.), 13, 15792
Öberg, K. I., van Broekhuizen, F., Fraser, H. J., et al. 2005, ApJ, 621, L33
Öberg, K. I., van Dishoeck, E. F., & Linnartz, H. 2009, A&A, 496, 281
Palumbo, M. E., Baratta, G. A., Brucato, J. R., et al. 1998, A&A, 334, 247
Pontoppidan, K. M., Fraser, H. J., Dartois, E., et al. 2003, A&A, 408, 981
Pontoppidan, K. M., Boogert, A. C. A., Fraser, H. J., et al. 2008, ApJ, 678, 1005
Raut, U., & Baragiola, R. A. 2011, ApJ, 737, L14
Raut, U., Fulvio, D., Loeffler, M. J., & Baragiola, R. A. 2012, ApJ, 752, 159
Roser, J. E., Vidali, G., Manicò, G., & Pirronello, V. 2001, ApJ, 555, L61
Sabri, T., Baratta, G. A., Jäger, C., et al. 2015, A&A, 575, A76
Sandford, S. A., Allamandola, L. J., Tielens, A. G. G. M., & Valero, G. J. 1988, ApJ, 329, 498
Santos, J. C., Chuang, K.-J., Lamberts, T., et al. 2022, ApJ, 931, L33
Schriever, R., Chergui, M., & Schwentner, N. 1990, J. Chem. Phys., 93, 9206
Schwarz, K. R., Bergin, E. A., Cleeves, L. I., et al. 2016, ApJ, 823, 91
Shi, J., Grieves, G. A., & Orlando, T. M. 2015, ApJ, 804, 24
Stief, L. J., Payne, W. A., & Klemm, R. B. 1975, J. Chem. Phys., 62, 4000
Trapman, L., Miotello, A., Kama, M., van Dishoeck, E. F., & Bruderer, S. 2017, A&A, 605, A69
Trapman, L., Bosman, A. D., Rosotti, G., Hogerheijde, M. R., & van Dishoeck, E. F. 2021, A&A, 649, A95
van Broekhuizen, F. A., Groot, I. M. N., Fraser, H. J., van Dishoeck, E. F., & Schlemmer, S. 2006, A&A, 451, 723
van Dishoeck, E. F., Bergin, E. A., Lis, D. C., & Lunine, J. I. 2014, in Protostars and Planets VI, eds. H. Beuther, R. S. Klessen, C. P. Dullemond, & T. Henning, 835
Virtanen, P., Gommers, R., Oliphant, T. E., et al. 2020, Nat. Methods, 17, 261
Watanabe, N., & Kouchi, A. 2002a, ApJ, 571, L173
Watanabe, N., & Kouchi, A. 2002b, ApJ, 567, 651
Watanabe, N., Nagaoka, A., Shiraki, T., & Kouchi, A. 2004, ApJ, 616, 638
Watanabe, N., Mouri, O., Nagaoka, A., et al. 2007, ApJ, 668, 1001
Whittet, D. C. B., Gerakines, P. A., Hough, J. H., & Shenoy, S. S. 2001, ApJ, 547, 872
Whittet, D. C. B., Goldsmith, P. F., & Pineda, J. L. 2010, ApJ, 720, 259
Yuan, C., Cooke, I. R., & Yates, John T. J. 2014, ApJ, 791, L21
Zins, E.-L., Joshi, P. R., & Krim, L. 2011, ApJ, 738, 175

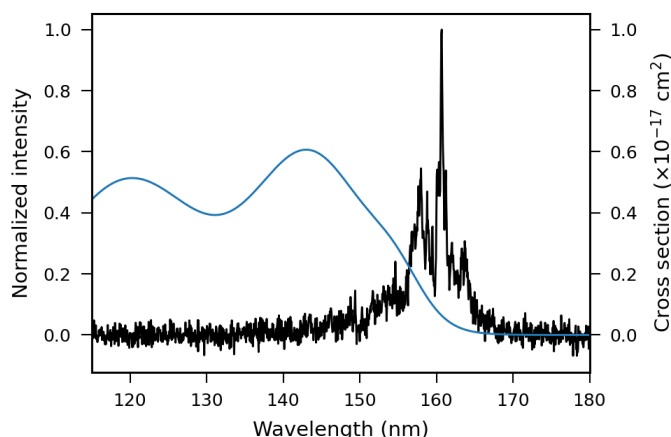**Fig. A.1.** Black: In-situ measured VUV spectrum of the microwave-discharge hydrogen-flow lamp used in combination with a MgF$_2$ window that absorbs Lyman-α. Blue: solid-state H$_2$O VUV absorption cross section as function of wavelength taken from Cruz-Diaz et al. (2014).

Appendix A: VUV spectrum

The spectral energy distribution of the MDHL used in this study is measured in situ with a VUV spectrometer (McPherson Model 234/302), which is mounted opposite to the MDHL on the other side of the main chamber. In this work a MgF$_2$ window was used that does not transmit Lyman-α photons, but does transmit the molecular hydrogen emission lines and continuum between 140–170 nm. The VUV absorption cross section as a function of wavelength is taken from literature (Cruz-Diaz et al. 2014). It is the summation of three Gaussians with the parameters taken from their Table 2. Both the VUV spectrum with which the ASW is irradiated and the wavelength dependent H$_2$O VUV absorption cross section are shown in Fig. A.1.

Appendix B: Additional experiments

The main experiments at 50, 60, 80, 90, 100, and 120 K and control experiments with ^{13}CO instead of ^{13}C^{18}O, no VUV irradiation, and no gas-phase CO in the chamber during VUV irradiation are presented in this appendix. In the majority of the experiments there is an artifact in the QMS data during TPD, as can be seen in for example Fig. B.1d. This is the result of a nonlinear temperature increase in the sample, which is likely caused by a change in thermal conductivity or contact between the sample and heating strip. The LakeShore PID controller compensates for this, but results in a brief period of undershoot followed by overshoot of the sample temperature. This occurs approximately in the temperature range 120–150 K. In the caption of each figure the exact temperature range is given in which the QMS signals are not accurately representing what the TPD should look like if the temperature increase were to be fully linear.
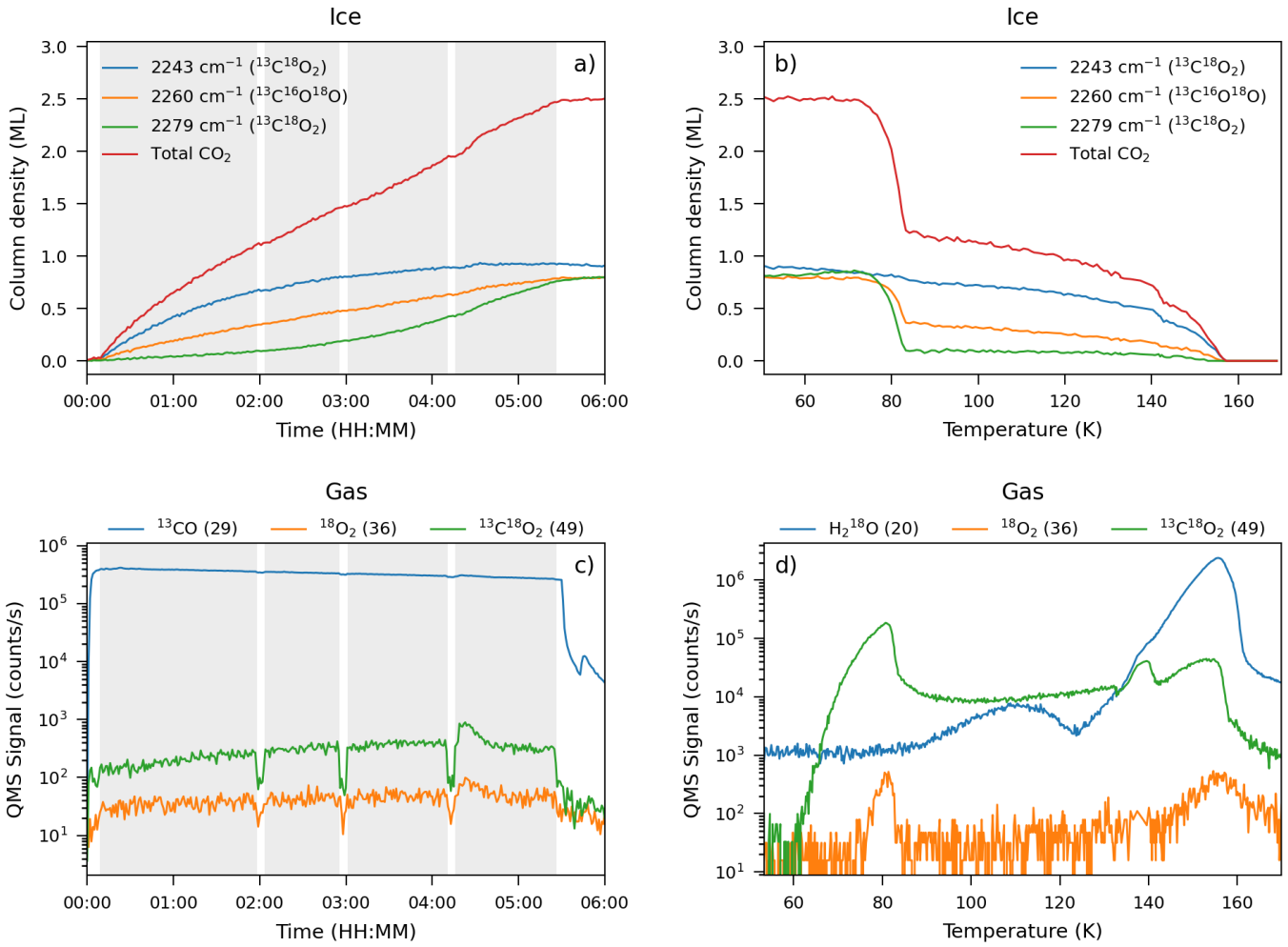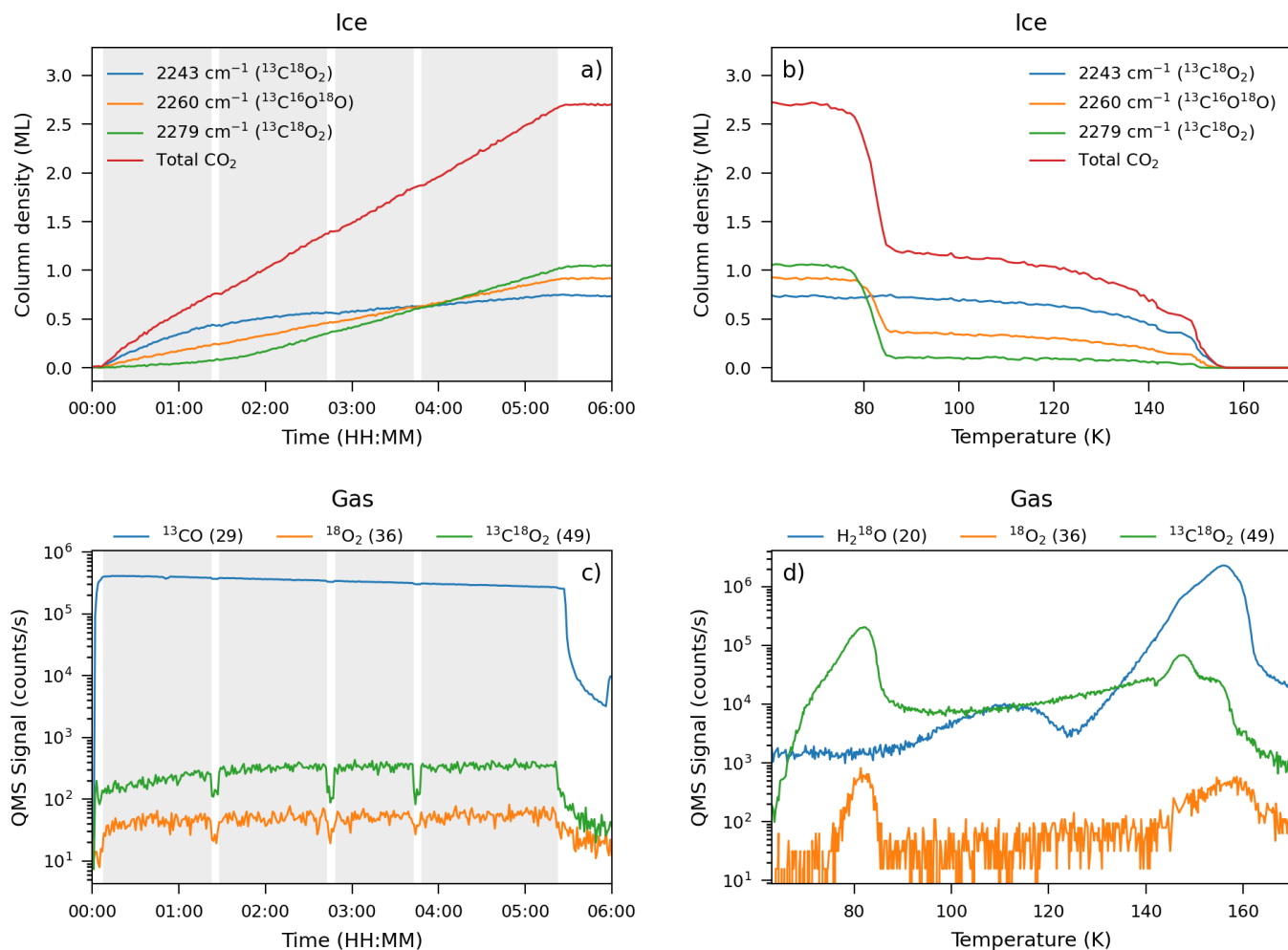
Fig. B.1. Results of the experiment of ASW at a temperature of 50 K. In the top row the deconvolved infrared components, which trace the solid state, are given, based on RAIRS during VUV irradiation (panel a) and temperature programmed desorption (TPD) in panel b). In the *bottom row* the data from the quadrupole mass spectrometer (QMS) is presented, which trace the gas phase. The *left column* shows data acquired during VUV irradiation (shaded areas indicate when the VUV shutter is open) and on the right during TPD. In panel c) ^{13}CO is shown, as measuring the main isotopologue ($^{13}C^{18}O$) would saturate the QMS. The ^{16}O isotope is present in the CO sample at a level of 5%. The TPD QMS data in panel d) between 130–140 K is unreliable due to a nonlinear temperature artifact during heating of the sample.
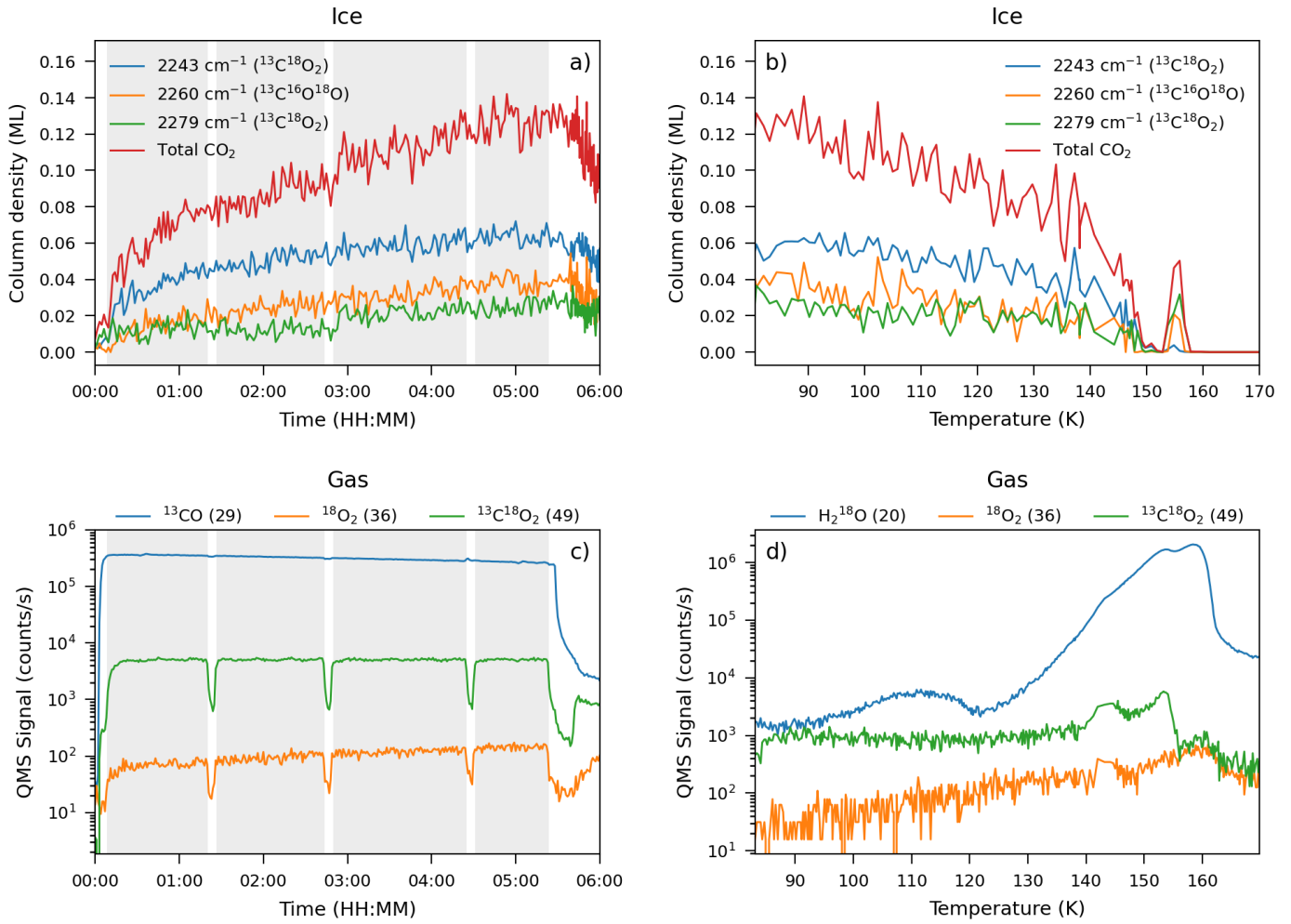
Fig. B.2. Results of the experiment of ASW at a temperature of 60 K. In the top row the deconvolved infrared components, which trace the solid state, are given, based on RAIRS during VUV irradiation (panel a) and temperature programmed desorption (TPD) in panel b). In the bottom row the data from the quadrupole mass spectrometer (QMS) is presented, which trace the gas phase. The left column shows data acquired during VUV irradiation (shaded areas indicate when the VUV shutter is open) and on the right during TPD. In panel c) ^{13}CO is shown, as measuring the main isotopologue ($^{13}C^{18}O$) would saturate the QMS. The ^{16}O isotope is present in the CO sample at a level of 5%. The TPD QMS data in panel d) between 140–150 K is unreliable due to a nonlinear temperature artifact during heating of the sample.
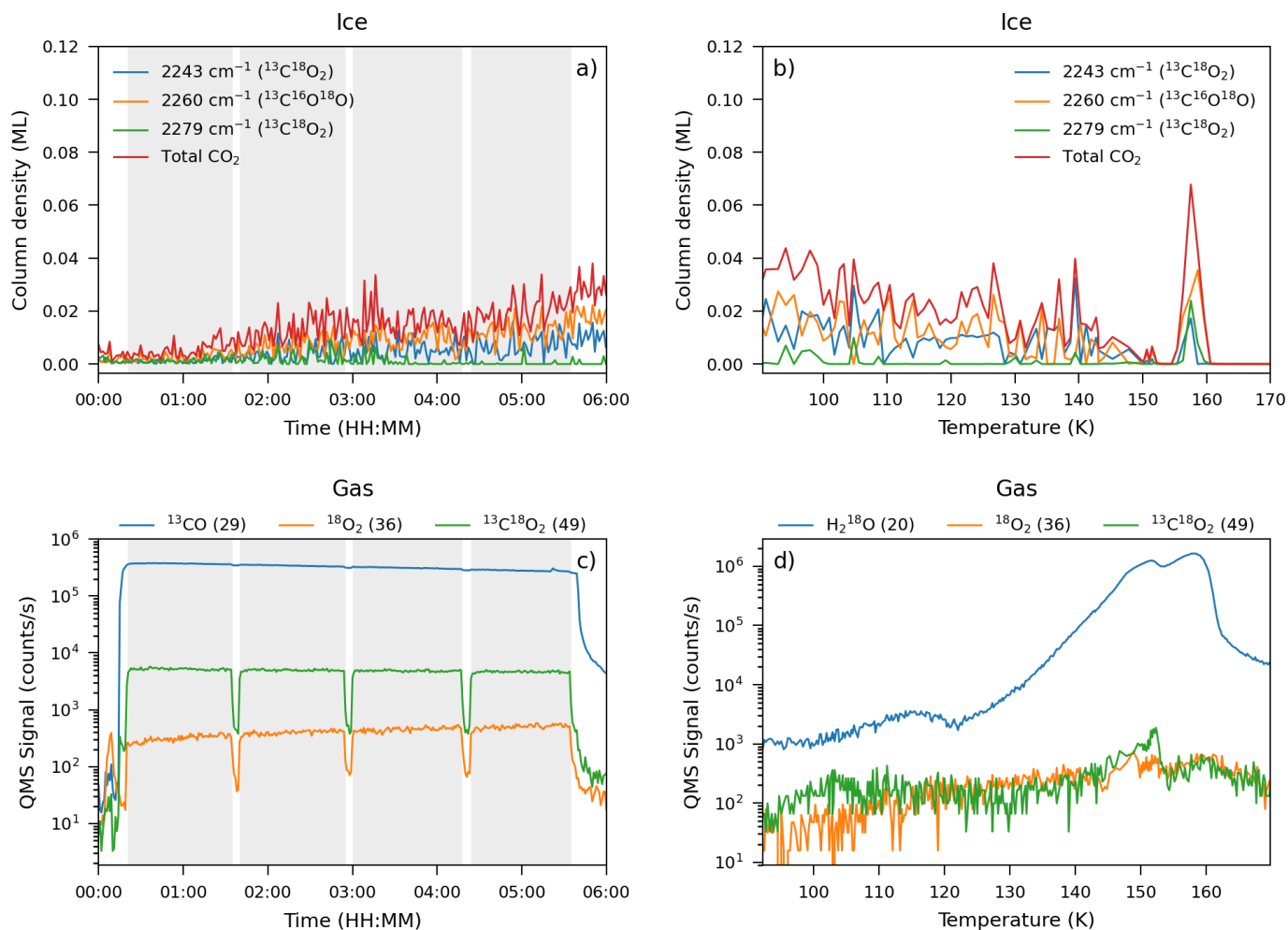
Fig. B.3. Results of the experiment of ASW at a temperature of 80 K. In the top row the deconvolved infrared components, which trace the solid state, are given, based on RAIRS during VUV irradiation (panel a) and temperature programmed desorption (TPD) in panel b). In the bottom row the data from the quadrupole mass spectrometer (QMS) is presented, which trace the gas phase. The left column shows data acquired during VUV irradiation (shaded areas indicate when the VUV shutter is open) and on the right during TPD. In panel c) ^{13}CO is shown, as measuring the main isotopologue ($^{13}C^{18}O$) would saturate the QMS. The ^{16}O isotope is present in the CO sample at a level of 5%. The TPD QMS data in panel d) between 140–150 K is unreliable due to a nonlinear temperature artifact during heating of the sample.
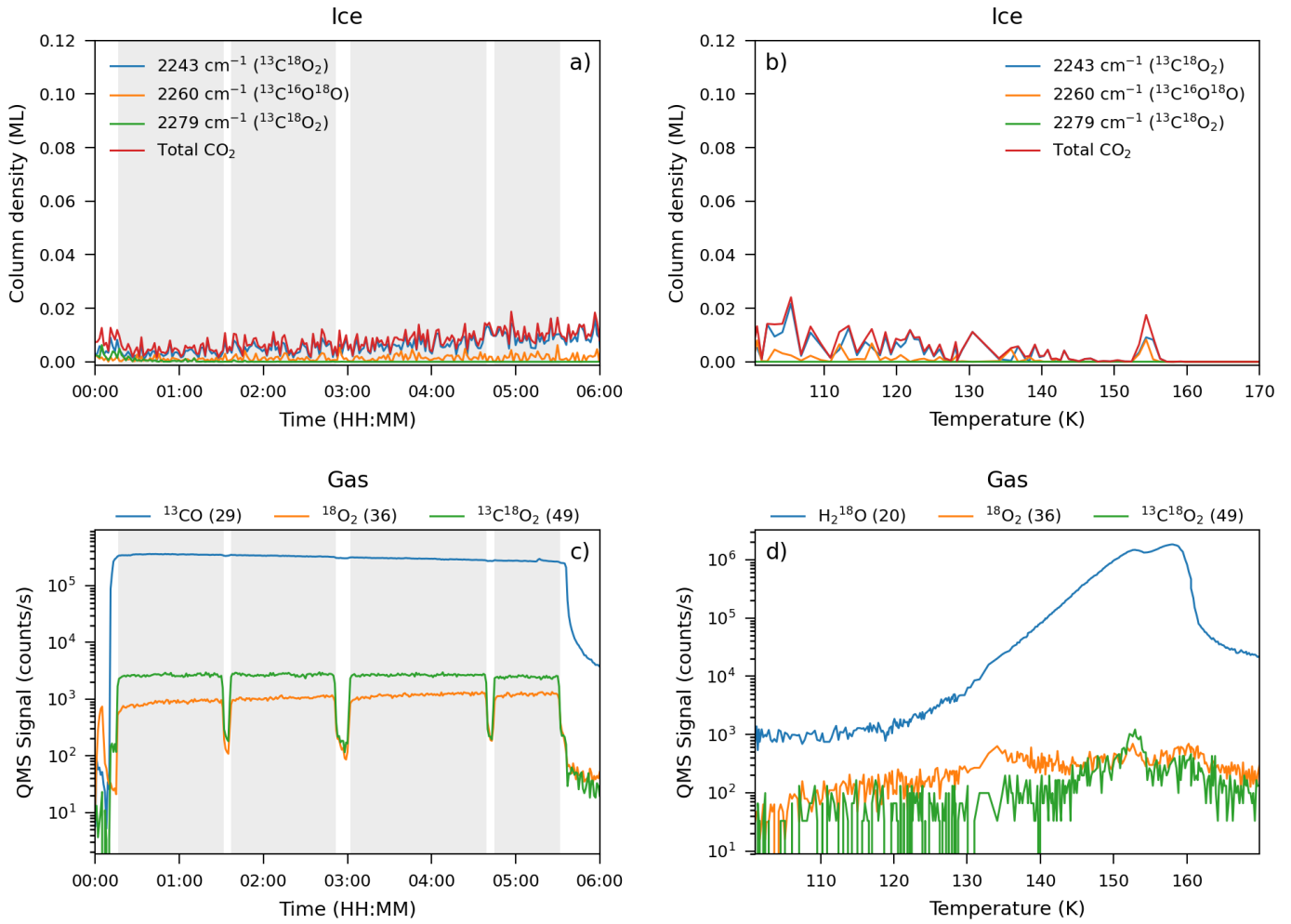
Fig. B.4. Results of the experiment of ASW at a temperature of 90 K. In the top row the deconvolved infrared components, which trace the solid state, are given, based on RAIRS during VUV irradiation (panel a) and temperature programmed desorption (TPD) in panel b). In the bottom row the data from the quadrupole mass spectrometer (QMS) is presented, which trace the gas phase. The left column shows data acquired during VUV irradiation (shaded areas indicate when the VUV shutter is open) and on the right during TPD. In panel c) ^{13}CO is shown, as measuring the main isotopologue (^{13}C^{18}O) would saturate the QMS. The ^{16}O isotope is present in the CO sample at a level of 5%.

Fig. B.5. Results of the experiment of ASW at a temperature of 100 K. In the top row the deconvolved infrared components, which trace the solid state, are given, based on RAIRS during VUV irradiation (panel a) and temperature programmed desorption (TPD) in panel b). In the bottom row the data from the quadrupole mass spectrometer (QMS) is presented, which trace the gas phase. The left column shows data acquired during VUV irradiation (shaded areas indicate when the VUV shutter is open) and on the right during TPD. In panel c) ^{13}CO is shown, as measuring the main isotopologue ($^{13}C^{18}O$) would saturate the QMS. The ^{16}O isotope is present in the CO sample at a level of 5%. The TPD QMS data in panel d) between 130–140 K is unreliable due to a nonlinear temperature artifact during heating of the sample.
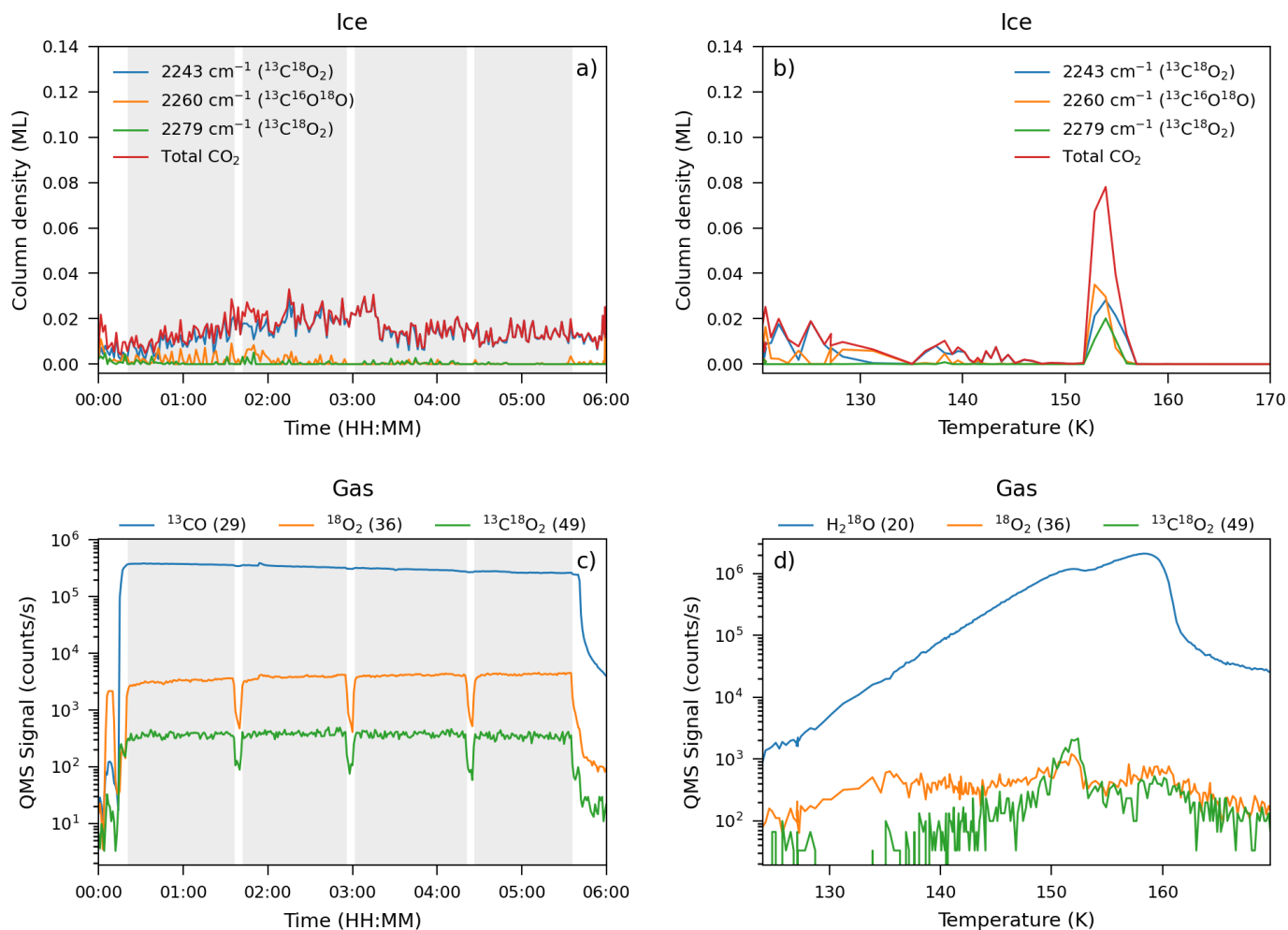
Fig. B.6. Results of the experiment of ASW at a temperature of 120 K. In the top row the deconvolved infrared components, which trace the solid state, are given, based on RAIRS during VUV irradiation (panel a) and temperature programmed desorption (TPD) in panel b). In the bottom row the data from the quadrupole mass spectrometer (QMS) is presented, which trace the gas phase. The left column shows data acquired during VUV irradiation (shaded areas indicate when the VUV shutter is open) and on the right during TPD. In panel c) ^{13}CO is shown, as measuring the main isotopologue (^{13}C^{18}O) would saturate the QMS. The ^{16}O isotope is present in the CO sample at a level of 5%. The TPD QMS data in panel d) between 130–140 K is unreliable due to a nonlinear temperature artifact during heating of the sample.
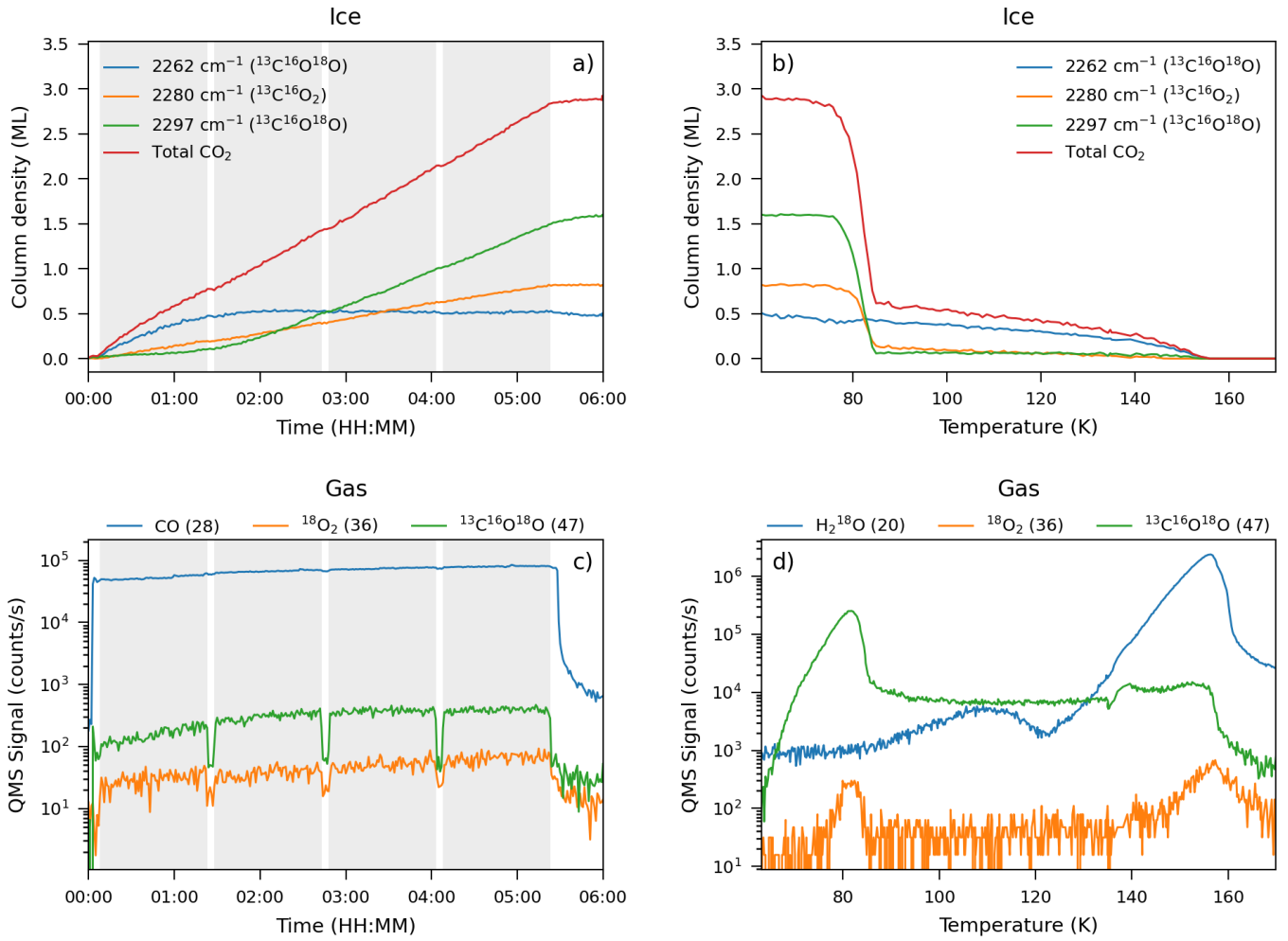
Fig. B.7. Results of the control experiment of ASW at a temperature of 60 K with the isotopologue $^{13}C^{16}O$ instead of $^{13}C^{18}O$. In the top row the deconvolved infrared components, which trace the solid state, are given, based on RAIRS during VUV irradiation (panel a) and temperature programmed desorption (TPD) in panel b). In the bottom row the data from the quadrupole mass spectrometer (QMS) is presented, which trace the gas phase. The left column shows data acquired during VUV irradiation (shaded areas indicate when the VUV shutter is open) and on the right during TPD. In panel c) ^{12}CO is shown, as measuring the main isotopologue (^{13}CO) would saturate the QMS. The ^{12}C isotope is present in the CO sample at a level of 1%. The TPD QMS data in panel d) between 130–140 K is unreliable due to a nonlinear temperature artifact during heating of the sample.
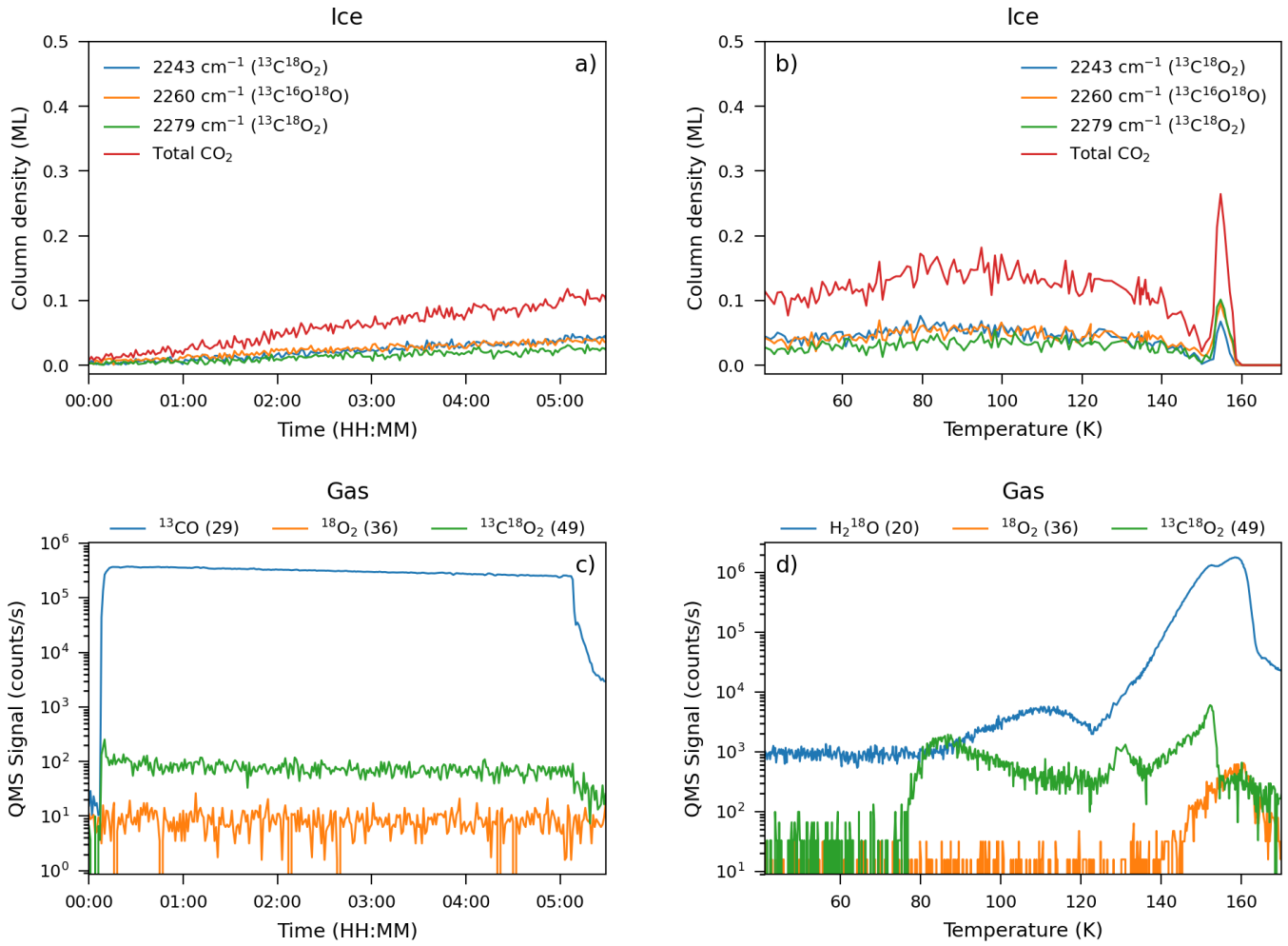
Fig. B.8. Results of the control experiment of ASW at a temperature of 40 K without VUV irradiation. In the top row the deconvolved infrared components, which trace the solid state, are given, based on RAIRS during VUV irradiation (panel a) and temperature programmed desorption (TPD) in panel b). In the bottom row the data from the quadrupole mass spectrometer (QMS) is presented, which trace the gas phase. The left column shows data acquired during VUV irradiation (shaded areas indicate when the VUV shutter is open) and on the right during TPD. In panel c) ^{13}CO is shown, as measuring the main isotopologue (^{13}C^{18}O) would saturate the QMS. The ^{16}O isotope is present in the CO sample at a level of 5%.
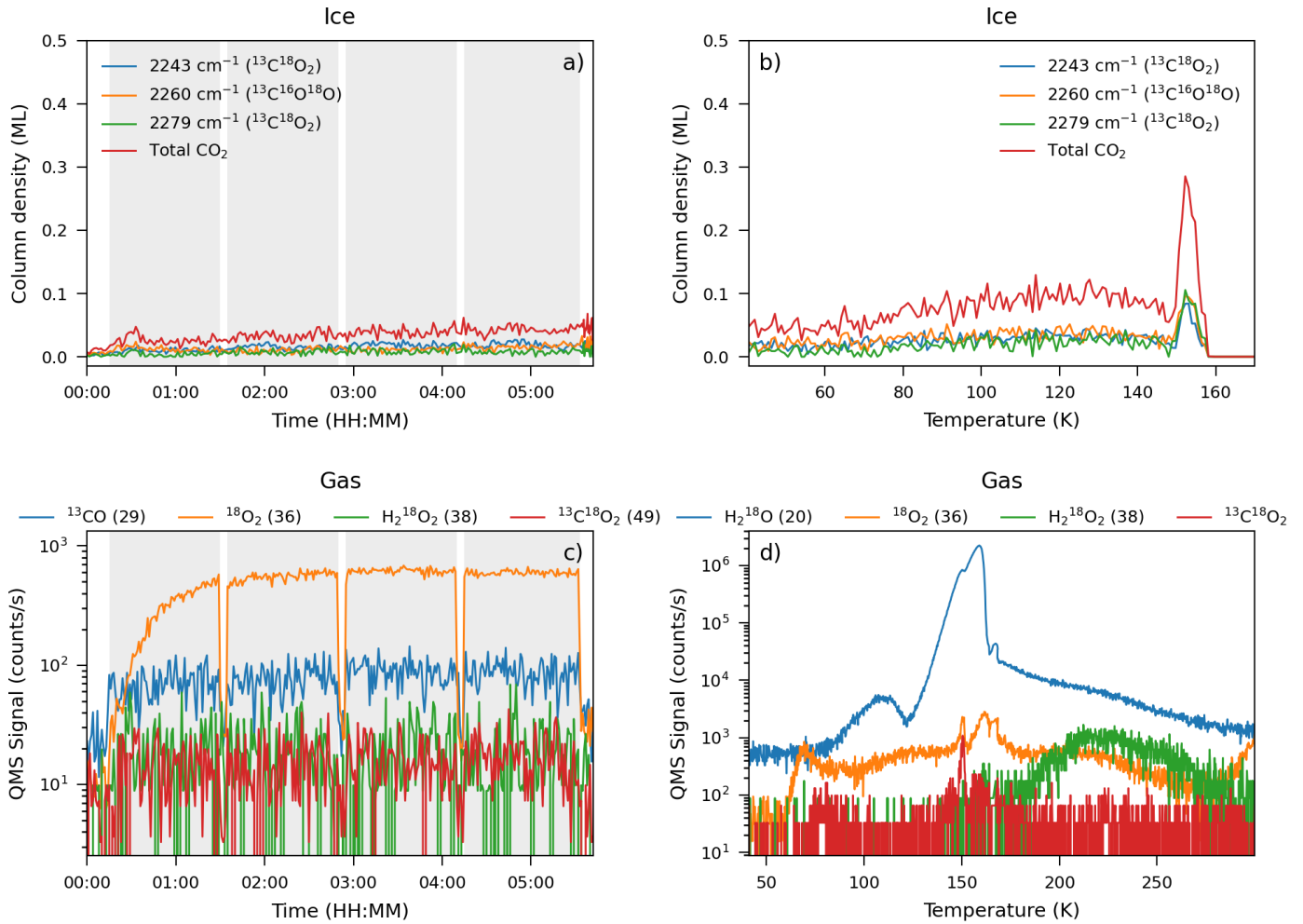
Fig. B.9. Results of the control experiment of ASW at a temperature of 40 K without gas-phase CO. In the top row the deconvolved infrared components, which trace the solid state, are given, based on RAIRS during VUV irradiation (panel a) and temperature programmed desorption (TPD) in panel b). In the bottom row the data from the quadrupole mass spectrometer (QMS) is presented, which trace the gas phase. The left column shows data acquired during VUV irradiation (shaded areas indicate when the VUV shutter is open) and on the right during TPD. TPD is now shown up until 300 K to show the desorption of H_2O_2. In panel c) ^{13}CO is shown, to verify that indeed no significant amount of CO is in the gas phase during VUV irradiation.